Nuclear Instruments and Methods in Physics Research A 592 (2008) 297–315

Contents lists available at ScienceDirect

Nuclear Instruments and Methods in Physics Research A

journal homepage: www.elsevier.com/locate/nima

The DAMA/LIBRA apparatus

R. Bernabei [a,b,*], P. Belli [b], A. Bussolotti [b], F. Cappella [c,d], R. Cerulli [e], C.J. Dai [f], A. d'Angelo [c,d], H.L. He [f], A. Incicchitti [d], H.H. Kuang [f], J.M. Ma [f], A. Mattei [d], F. Montecchia [a,b], F. Nozzoli [a,b], D. Prosperi [c,d], X.D. Sheng [f], Z.P. Ye [f,g]

[a] Dip. di Fisica, Università di Roma "Tor Vergata", I-00133 Rome, Italy
[b] INFN, sez. Roma "Tor Vergata", I-00133 Rome, Italy
[c] Dip. di Fisica, Università di Roma "La Sapienza", I-00185 Rome, Italy
[d] INFN, sez. Roma, I-00185 Rome, Italy
[e] Laboratori Nazionali del Gran Sasso, INFN, Assergi, Italy
[f] IHEP, Chinese Academy, P.O. Box 918/3, Beijing 100039, China
[g] University of Jing Gangshan, Jiangxi, China

ARTICLE INFO

Article history:
Received 11 February 2008
Received in revised form
28 February 2008
Accepted 27 April 2008
Available online 17 May 2008

Keywords:
Scintillation detectors
Elementary particle processes

ABSTRACT

The $\simeq 250$ kg highly radiopure NaI(Tl) DAMA/LIBRA apparatus, running at the Gran Sasso National Laboratory (LNGS) of the INFN, is described.

1. Introduction

While running the first generation DAMA/NaI apparatus ($\simeq 100$ kg highly radiopure NaI(Tl)) [1–12], DAMA proposed to realize a ton apparatus in 1996 [13]. Thus, a second generation R&D project for highly radiopure NaI(Tl) detectors was funded and carried out over several years with leader companies in order to realize, as a new step, a second generation experiment with an exposed mass of about 250 kg. The $\simeq 250$ kg highly radiopure NaI(Tl) DAMA/LIBRA (Large sodium Iodide Bulk for RAre processes) apparatus has been designed and built mainly to further investigate the Dark Matter particle component(s) in the galactic halo by exploiting the annual modulation signature; it also aims to improve the investigation of several rare processes. DAMA/NaI completed its data taking in July 2002 and the installation of DAMA/LIBRA started (see Fig. 1). DAMA/LIBRA has begun first operations in March 2003.

In the present paper, the DAMA/LIBRA apparatus and, in particular, the features of its new detectors, developed by means of the second generation R&D, are described.

2. The target material

Highly radiopure NaI(Tl) scintillators have been chosen as target—detector material for particle Dark Matter investigations since they offer many competitive aspects; among them we remind: (1) well-known technology; (2) high radiopurity reachable by material selections and protocols, by chemical/physical purifications, etc.; (3) large mass feasible; (4) high duty cycle; (5) routine calibrations feasible down to keV range in the same conditions as the production runs; (6) well controlled operational conditions and monitoring feasible; (7) absence of microphonic noise; (8) suitable signal/noise discrimination near the energy threshold profiting of the relatively high available number of photoelectrons/keV and of the well different timing structures of the PMT noise pulses (single fast photoelectrons with decay time of order of tens of ns) with respect to the NaI(Tl) scintillation pulses (time distribution with time decay of order of hundreds of ns); (9) high light response, that is keV threshold really reachable; (10) no necessity of re-purification or cooling down/warming up procedures (implying high reproducibility, high stability, etc.); (11) possibility to exploit the granularity of the apparatus, an interesting feature for Dark Matter particle investigations and for background recognition; (12) sensitivity to both high (by Iodine target) and low (by Na target) mass WIMP (Weakly Interacting Massive Particles) candidates;

---

[*] Corresponding author at: Dip. di Fisica, Università di Roma "Tor Vergata", I-00133 Rome, Italy. Tel./fax: +39 0672594542.
E-mail address: rita.bernabei@roma2.infn.it (R. Bernabei).

0168-9002/$ - see front matter © 2008 Elsevier B.V. All rights reserved.
doi:10.1016/j.nima.2008.04.082

Fig. 1. Disinstalling DAMA/NaI and installing DAMA/LIBRA; all procedures involving detectors, photomultipliers (PMTs), etc. have been carried out in HP (High Purity) Nitrogen atmosphere. Improving the experimental site (walls, floor, etc.) after removal of the DAMA/NaI electronics (*top left*); dismounting the DAMA/NaI detectors in HP Nitrogen atmosphere (*top right*); assembling a DAMA/LIBRA detector in HP Nitrogen atmosphere (*bottom left*); installing the DAMA/LIBRA detectors in HP Nitrogen atmosphere (*center right*) and a view of the inner Cu box filled by the DAMA/LIBRA detectors in HP Nitrogen atmosphere (*bottom right*).

(13) high sensitivity to the class of WIMP candidates with spin-independent (SI), spin-dependent (SD) and mixed (SI&SD) couplings (see e.g. Refs. [4,14]); (14) high sensitivity to several other existing scenarios (see e.g. Refs. [4–11,15]) and to many other possible candidates including those producing just electromagnetic radiation in the interaction; (15) possibility to effectively investigate the annual modulation signature in all the needed aspects; (16) "ecologically clean" apparatus, thus no safety problems; (17) technique cheaper than every other considered in the field; (18) small underground space needed; (19) pulse shape discrimination feasible at reasonable level when of interest.

Moreover, highly radiopure NaI(Tl) scintillators can also offer the possibility to achieve significant results on several other rare processes—as already done by the DAMA/NaI apparatus—such as e.g. [16]: (i) possible violation of Pauli exclusion principle in ^{127}I and in ^{23}Na; (ii) electron stability; (iii) charge non-conserving processes; (iv) search for solar axions; (v) search for exotic matter; (vi) search for spontaneous transition of nuclei to a superdense state; (vii) search for spontaneous emission of heavy clusters in ^{127}I; (viii) search for possible nucleon, di-nucleon and tri-nucleon decays into invisible channels; etc.

3. Layout of the experimental apparatus

The main parts of the experimental apparatus are: (i) the installation; (ii) the multicomponent passive shield; (iii) the 25 highly radiopure NaI(Tl) detectors; (iv) the glove-box for calibrations; (v) the electronic chain and the monitoring/alarm system; (vi) the data acquisition (DAQ) system.

All the materials constituting the apparatus have been selected for low radioactivity by measuring samples with low background Ge detector deep underground in the Gran Sasso National Laboratory and/or by Mass Spectrometry (MS) and by Atomic Absorption Spectroscopy (AAS).

3.1. The installation

A schematic view of the building housing the DAMA/LIBRA experimental apparatus is shown in Fig. 2. Even the materials, the paints, etc., used to build the installation, have been selected for low radioactivity as much as possible at time of construction. Most of the materials have been underground since about 15 years or more.

At the ground floor, the room D in Fig. 2 houses the computer devoted to the data acquisition and the room C contains the sensitive part of the apparatus, the passive shield, the electronic chain and the acquisition system. The floor and the walls of the room C are sealed from external air by a tight coverage made by Supronyl (permeability equal to 2×10^{-11} cm^2/s [17]); this is the first level of sealing from the Radon present in trace in the air of the underground laboratory. The door at entrance of the room C is air tight and—since HP Nitrogen is released in this room—a low level oxygen alarm is in operation. The level of the environmental Radon inside the experimental room C is continuously monitored by a Radon-meter and recorded with the production data; it shows that the environmental Radon in the installation is at level of the Radon-meter sensitivity ($\simeq 3$ Bq/m^3).

The DAMA/LIBRA passive shield is supported by a metallic structure mounted above a concrete basement (see Fig. 2). A neoprene layer separates the concrete basement and the floor of the laboratory. The space between this basement and the metallic structure is filled by paraffin for several tens cm in height. This shield is sealed in a plexiglass box maintained in HP Nitrogen atmosphere in slight overpressure with respect to its external environment; this is the second level of sealing from the external air.

Two mechanical systems allow the lowering of the front and the back sides of the shield through an electric engine and, hence, to access the detectors during their installation (also see Fig. 1).

On the top of the shield (at the first floor, room A) a glove-box (also continuously maintained in the HP Nitrogen atmosphere) is directly connected through Cu pipes to the inner Cu box, housing the detectors. The inner Cu box is also continuously flushed with HP Nitrogen and maintained in slight overpressure with respect to its external environment (this is the third level of sealing from external air in the underground laboratory). The pipes are filled with low radioactivity Cu bars (covered by 10 cm of low radioactive Cu and 15 cm of low radioactive Pb) which can be removed to allow the insertion of radioactive sources holders for calibrating the detectors in the same running condition without any contact with the installation environment. The glove-box is also equipped with a compensation chamber.

Paraffin/polyethylene fill the space surrounding the plexiglass box as much as possible depending on the available space. Moreover, mostly outside the building, the DAMA/LIBRA apparatus is almost fully surrounded by about 1 m concrete made from the Gran Sasso rock material.

The whole installation is under air conditioning to assure a suitable and stable working temperature for the electronics. The huge heat capacity of the multi-tons passive shield ($\approx 10^6$ cal/°C) assures further a relevant stability of the detectors' operating temperature. In particular, two independent systems of air conditioning are available for redundancy: one cooled by water refrigerated by a devoted chiller and the other operating with cooling gas.

A hardware/software monitoring system provides data on the operating conditions. In particular, several probes are read out and the results are stored with the production data. A schematic view of the monitoring/alarm system is reported in Fig. 3. It is directly interfaced to the safety system of the laboratory, for prompt action of the LNGS operator. Moreover, self-controlled computer processes automatically monitor several parameters—including those from DAQ—and manage alarms (by e-mails and by SMS) to the DAMA operator if one of them would go out of the allowed range (whose restrictions depend on the required stability level of the running conditions).

4. The shield from environmental radioactivity

Fig. 4(a) shows a schematic view of the Cu/Pb/Cd/polyethylene-paraffin low background hard shield against environmental radioactivity made of very high radiopure materials, which are underground since at least about 15 years. Moreover, paraffin/polyethylene fill the space surrounding the plexiglass box as much as possible depending on the available space and, as mentioned, mostly outside the building, the DAMA/LIBRA apparatus is almost

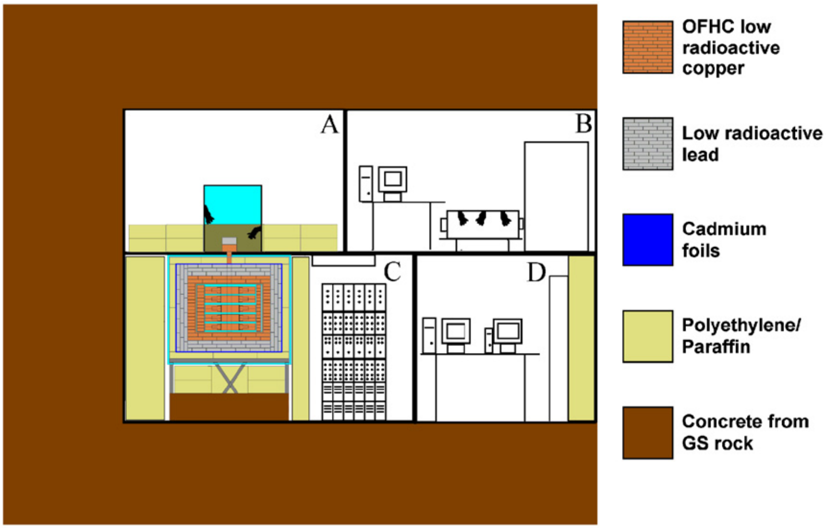

Fig. 2. Schematic view of the building hosting the DAMA/LIBRA apparatus (not to scale). About 1 m concrete (made from the Gran Sasso rock material) almost fully surrounds (mostly outside the building) the apparatus. In particular, the room A hosts the glove-box for calibrations; some facilities are in the room B; the sensitive parts of the apparatus are in the room C inside the multi-component shield as well as the electronics; the computer for DAQ is in the room D.

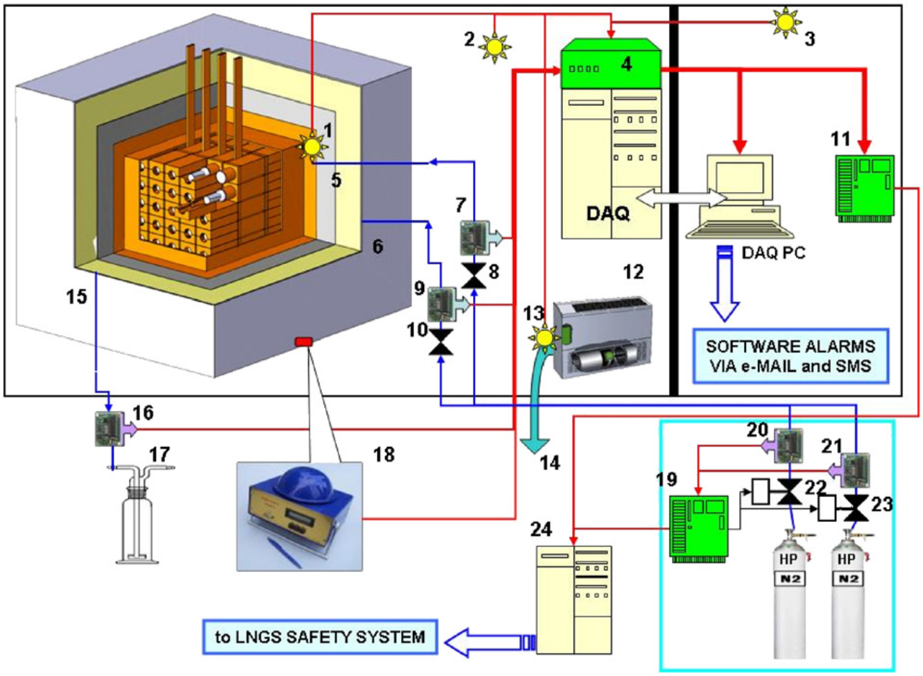

Fig. 3. A schematic and simplified view of the monitoring/alarm system. (1) Temperature probe of the detectors' environment; (2) temperature probes of the electronic devices; (3) temperature probe of the DAQ system; (4) interface of the probes; (5) HP N_2 gas inlet in the inner CU box; (6) HP N_2 gas inlet in the external plexiglass box; (7) and (9) fluxmeters; (8) and (10) valves for the flux regulating; (11) interface towards the LNGS alarm system; (12) fan coil; (13) temperature probe for the water in the cooling system; (14) cooling system towards a chiller; (15) gas outlet; (16) pressure gauge; (17) gas bubbler; (18) Radon meter; (19) interface of the control of the gas bottles; (20) and (21) pressure meters; (22) and (23) electrovalves; (24) local junction box of the safety and alarm system of LNGS. Moreover, self-controlled computer processes automatically monitor also several other parameters (the above mentioned and those from the DAQ) and manage software alarms (by e-mails and by SMS) to operator.

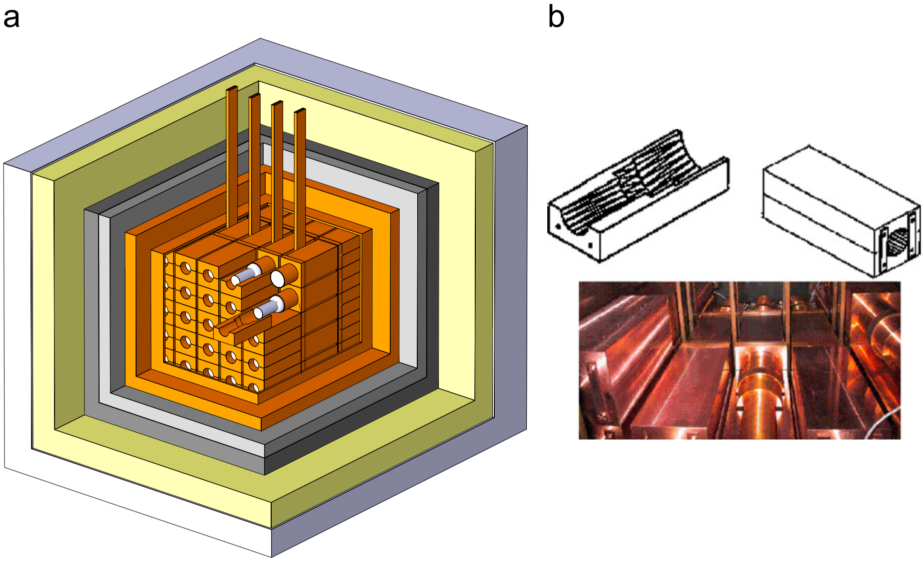

Fig. 4. (a) A schematic view of the passive shield of the DAMA/LIBRA apparatus. Mostly outside the installation, the DAMA/LIBRA apparatus is also almost fully surrounded by about 1 m concrete made of the Gran Sasso rock. (b) *Up*: A scheme of the shaped low-radioactivity copper shield for the PMTs; *down*: detectors during installation; in the central and right up detectors the new shaped Cu shield surrounding light guides and PMTs was not yet applied. See text.

fully surrounded by about 1 m concrete, made from the Gran Sasso rock, which acts as a further neutron moderator.[1]

The 25 highly radiopure NaI(Tl) detectors are placed in 5 rows × 5 columns. Each one has 9.70 kg mass and the size is $10.2 \times 10.2 \times 25.4\,\text{cm}^3$. They constitute the sensitive part of the DAMA/LIBRA apparatus and together with the PMTs (two for each detector at opposite sides) and their Cu shields are enclosed in a sealed low radioactive OFHC Cu box continuously flushed with HP N_2 longly stored deep underground (see Fig. 5). The Cu box is maintained at small overpressure with the respect to the environment, such as also the glove-box on the upper level (see Fig. 2).

In the DAMA/LIBRA apparatus the PMTs and their 10 cm long light guides (made of Suprasil B [22] and directly coupled to the

---

[1] Neutron fluxes measured deep underground in the Gran Sasso National Laboratory in the various energy regions are reported in Refs. [18–21].

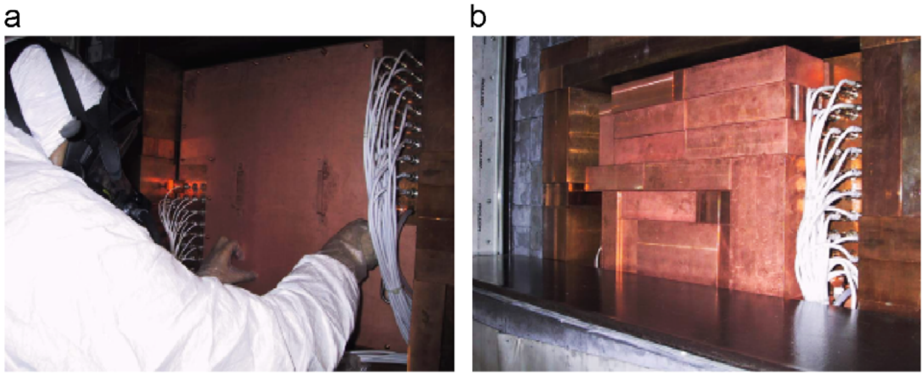

Fig. 5. (a) Sealing the low radioactive OFHC Cu box. (b) The space in front of the Cu box is filled by low radioactive Cu bricks and the front wall of the shield can go up.

bare crystal acting also as optical windows) are surrounded by shaped low-radioactive OFHC freshly electrolyzed copper shields; see Fig. 4(b).

All the materials constituting the Cu box and the Cu bricks, used to fill it as much as possible, have been selected for low radioactivity. Particular care has been devoted to the long-living so-called standard contaminants: ^{238}U, ^{232}Th and ^{40}K, since the first two have very rich chains and the latter one is present at a level of 0.0117% in the ^{nat}K, which is very abundant in nature.

The residual radioactivity in some components of the Cu box, that houses the NaI(Tl) detectors, is: (i) in the copper: <0.5 ppb, <1 ppb and <0.6 ppm of ^{238}U, ^{232}Th and ^{nat}K, respectively; (ii) in the feedthroughs: <1.6 ppb and <1.8 ppm of ^{232}Th and ^{nat}K, respectively; (iii) in the neoprene used in O-ring: <54 ppb and <89 ppm of ^{232}Th and ^{nat}K, respectively. All the limits—at the level of sensitivity of the used Ge detector—are at 95% C.L.

Outside the Cu box, the passive shield is made by $\gtrsim 10$ cm of OFHC low radioactive copper, 15 cm of low radioactive lead, 1.5 mm of cadmium and about 10–40 cm of polyethylene/paraffin (thickness fixed by the available space); see Fig. 4(a). The residual contaminants in some components of the passive shield are (95% C.L.): (i) in the copper see before; (ii) in the Boliden Lead: <8 ppb, <0.03 ppb and <0.06 ppm of ^{238}U, ^{232}Th and ^{nat}K, respectively; (iii) in the Boliden2 Lead: <3.6 ppb, <0.027 ppb and <0.06 ppm of ^{238}U, ^{232}Th and ^{nat}K, respectively; (iv) in the Polish Lead: <7.4 ppb, <0.042 ppb and <0.03 ppm of ^{238}U, ^{232}Th and ^{nat}K, respectively; (v) in the polyethylene: <0.3 ppb, <0.7 ppb and <2 ppm of ^{238}U, ^{232}Th and ^{nat}K, respectively; (vi) in the plexiglass: <0.64 ppb, <27.2 ppb and <3.3 ppm of ^{238}U, ^{232}Th and ^{nat}K, respectively.

As mentioned, a sealed plexiglass box (also continuously flushed with HP Nitrogen gas) encloses the passive shield. The Supronyl coverage (see above) and the mentioned about 1 m concrete complete the DAMA/LIBRA shield. The sealed Cu box, the plexiglass box (both flushed with HP N_2) and the Supronyl represent the three-level sealing system from environmental air in the laboratory. Moreover, the Radon level inside the installation (that is just after the first more external level of sealing from external air) is continuously monitored and it is at the level of sensitivity of the Radon-meter; it is continuously recorded with the production data.

Specific procedures for preparing and handling the lead and copper bricks have also been selected. In particular, they have been chemically etched in a class 1000 clean room by using, respectively, HNO_3 and HCl aqueous solution in iper-pure water (conductivity $= 0.0548\,\mu$S/cm at 25 °C). As an example, the main steps followed for the inner Cu etching are summarized here: (i) Vessel I: pre-washing of the brick in iper-pure water; (ii) Vessel II: washing in 1.5 l of super-pure HCl 3 M; (iii) Vessel III: first rinse with iper-pure water (bath); (iv) Vessel IV: second rinse with iper-pure water (current); (v) Vessel V: washing in 1.5 l of ultra-pure HCl 0.5 M; (vi) Vessel VI: first rinse with iper-pure water (bath); (vii) Vessel VII: second rinse with iper-pure water (current); (viii) Vessel VIII: third rinse with iper-pure water (current); (ix) The Cu brick is dried with selected clean towels and HP N_2 flux; (x) Finally, the Cu brick is sealed in two envelopes (one inside the other) previously flushed and filled with HP N_2 and stored underground until their mounting. The residual contaminants in the HCl used in solution with iper-pure water are certified by the producer. In particular, standard contaminants are quoted to be: 10 ppb of ^{nat}K and 1 ppb of U/Th for super-pure HCl and 100 ppt of ^{nat}K and 1 ppt of U/Th for ultra-pure HCl. For each brick the bath was changed and after each step the solution of the bath was analyzed with ICP-MS technique. Residual contaminants were preliminarily checked in order to optimize the choice of the materials (in particular for gloves) and the cleaning procedure. Moreover, special tools have been built (by using teflon and high radiopure OFHC copper) to manage the bricks in order to minimize the contact with gloves in presence of acid solution. ICP-MS measurements assure the same radiopurity characteristics of the iper-pure water used in the last rinse, before and after the rinse.

5. The new highly radiopure NaI(Tl) detectors

The $\simeq 250$ kg NaI(Tl) DAMA/LIBRA apparatus uses 25 NaI(Tl) highly radiopure detectors with 9.70 kg mass each one ($10.2 \times 10.2 \times 25.4\,\mathrm{cm}^3$ volume) placed in five rows by five columns. The granularity of the apparatus is an interesting feature for Dark Matter particle investigations since Dark Matter particles can just contribute to events where only one of the 25 detectors fires (*single-hit* events) and not to whose where more than one detector fire in coincidence (*multiple-hit* events).

The new DAMA/LIBRA detectors have been built by Saint Gobain Crystals and Detectors company. The constituting materials have been selected by using several techniques; moreover, chemical/physical purifications of the selected powders have been exploited. In addition, the more effective growing procedure has been applied and new rules for handling the bare crystals have been fixed. Each detector is sealed in low radioactivity freshly electrolyzed copper housing and has two 10 cm long highly radiopure quartz (Suprasil B) light guides which also act as optical windows being directly coupled to the bare crystals.

The bare crystals have been built by Kyropoulos method [23] in a platinum crucible according to a strict growing and handling protocol developed and agreed under confidential restriction.[2] The seed, used in the growing, was from previous growth for highly radiopure NaI(Tl). The Kyropoulos method—following the specific protocol agreed with the Saint Gobain Crystals and Detectors company—has been adopted since it assures in particular: (i) possibility to operate in a well controlled overall situation for (radio)purity; (ii) significant (radio)purification during the growing process; (iii) high performances of the detectors. Other growing processes for NaI(Tl), such as the Bridgeman [23] was tested in the past and abandoned since it offered in our experience lower performances, mainly as regards the (radio)purification during growth.

The used NaI powders have preliminarily been selected for radiopurity by various methods; then, chemical/physical procedures for the further radiopurification have been exploited by Saint Gobain Crystals and Detectors company. The final residual contaminants in the powders are 0.02 ppb for ^{238}U, 0.02 ppb for ^{232}Th and <0.1 ppm (95% C.L.) for ^{nat}K, respectively, as measured by MS and AAS. As regards the selected TlI powder, the residual contaminants in the powders after the chemical/physical purifications are 0.8 ppb for ^{238}U, 1.2 ppb for ^{232}Th and <0.06 ppm (95% C.L.) for ^{nat}K, respectively, as measured by MS and AAS. It is worth noting that the concentration of Tl in the detectors is about 0.1%. Moreover, the growth with Kyropoulos method in platinum crucible with a peculiar devoted protocol acts as a further relevant radiopurification step. Obviously, the maximal sensitivity to determine the final residual contaminations is reached when directly measured in the crystals themselves (see later). In fact, the AAS and MS are mainly limited by the radiopurity of the line and by the added materials and—as mentioned—the used crystallization process itself acts as an additional considerable purification step. However, it is worth noting that the reachable final levels depend both on the initial impurity concentrations and on the used processes and handling protocols. Particular care has been devoted to the selection of tools and abrasives to be used for cutting and polishing the crystals from the produced large ingots; this requires, in particular, severe selections and control of tools and of procedures in order to avoid any significant pollution on surface during the operation.

The number of materials entering in the production and in the assembling of a detector—after the ingots production—has been minimized and deeply selected for radiopurity. In particular, selected Tetratec-teflon foils, wrapping the bare crystals, have been used as diffusers of the scintillation light because of their suitable performances and mainly of their radiopurity with respect to other possibilities. For the same reason, OFHC freshly electrolyzed copper has been used for the housings of the detectors. Preliminary suitable etching of the copper housings has been performed for a deep cleaning of possible residuals from machinery. Obviously, the foam (not distinguishable from outside by eyes), usually used inside the housing of standard NaI(Tl) detectors for compensation, is not used in the construction of the DAMA/LIBRA detectors because of the low background requirements. Instead, a mechanical compensation for the different specific heats of the Cu and NaI(Tl) is included in the design of the copper housing to avoid any possible damages during transportation in non-air-conditioned environment before installation deep underground. Many other specific expedients have also been exploited. In particular, we remind that the detectors, built for the DAMA apparata in Gran Sasso, have always been cut and assembled just after the growth of the crystalline bulk in a glove-box in controlled atmosphere, tightly sealed according to special requirements, road transported and immediately brought underground.

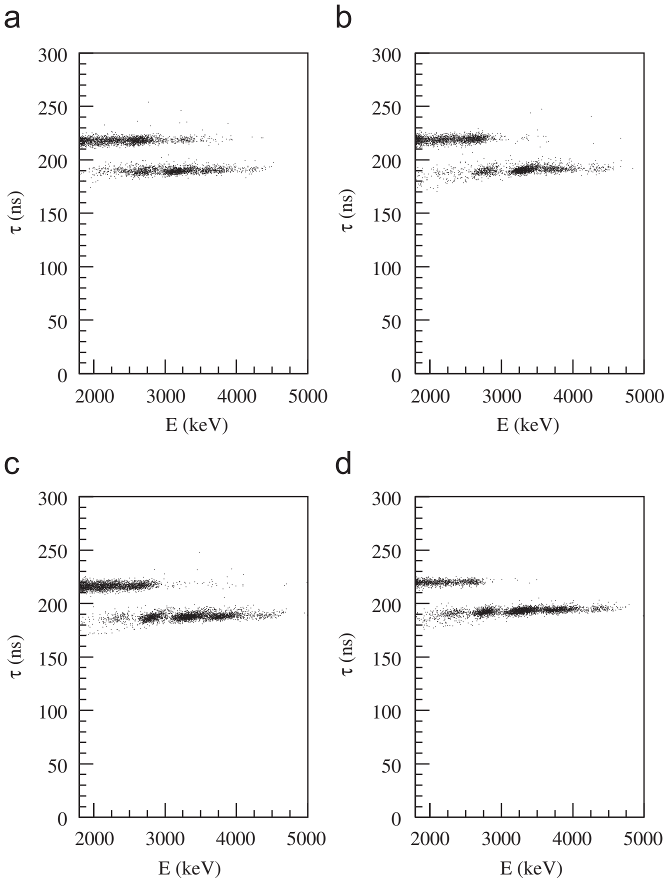

Fig. 6. First moment, τ, of the time distribution for each event (recorded by the Waveform Analyzer)—calculated within a 600 ns averaging time—as a function of the energy in unit of keV electron equivalent for four DAMA/LIBRA detectors. The two populations γ/e and α's are clearly separated; the α's have shorter τ's.

A preliminary estimate of the residual U and Th contamination in a detector can be obtained from the internal α particles produced by both chains. They can be measured by exploiting the α/e pulse shape discrimination in NaI(Tl), which has practically 100% effectiveness in the MeV range. Fig. 6 shows some examples of the distribution of τ as a function of energy for four DAMA/LIBRA detectors. The variable $\tau = \Sigma_i h_i t_i / \Sigma_i h_i$ is the first moment of the time distribution of each scintillation pulse (as recorded by the Waveform Analyzer; see Section 7); there h_i is the pulse height at the time t_i and the sum is over 600 ns after the starting of the pulse. The two populations γ/e and α's are clearly separated; the α particles have shorter τ values. The measured α yield in the DAMA/LIBRA detectors ranges from 7 to some tens α/kg/day.

5.1. ^{232}Th

The time–amplitude method[3] has been used to determine the activity of the ^{228}Th ($T_{1/2} = 1.912$ yr) subchain in the ^{232}Th family. In fact, the arrival time and energy of the events in each crystal can be used to identify a sequence of fast α decays following ^{228}Th decay: ^{224}Ra ($Q_\alpha = 5.789$ MeV, $T_{1/2} = 3.66$ d) $\rightarrow$

---

[2] The confidential agreement protects the intellectual properties both of the company and of the collaboration on the specific technical details.

[3] The technique of the time–amplitude analysis is based on the identification of radioactive isotopes by means of the characteristic time sequence of peculiar events (α, β, γ of known energy) given by the subsequent decays of daughter nuclides; see e.g. Ref. [24].

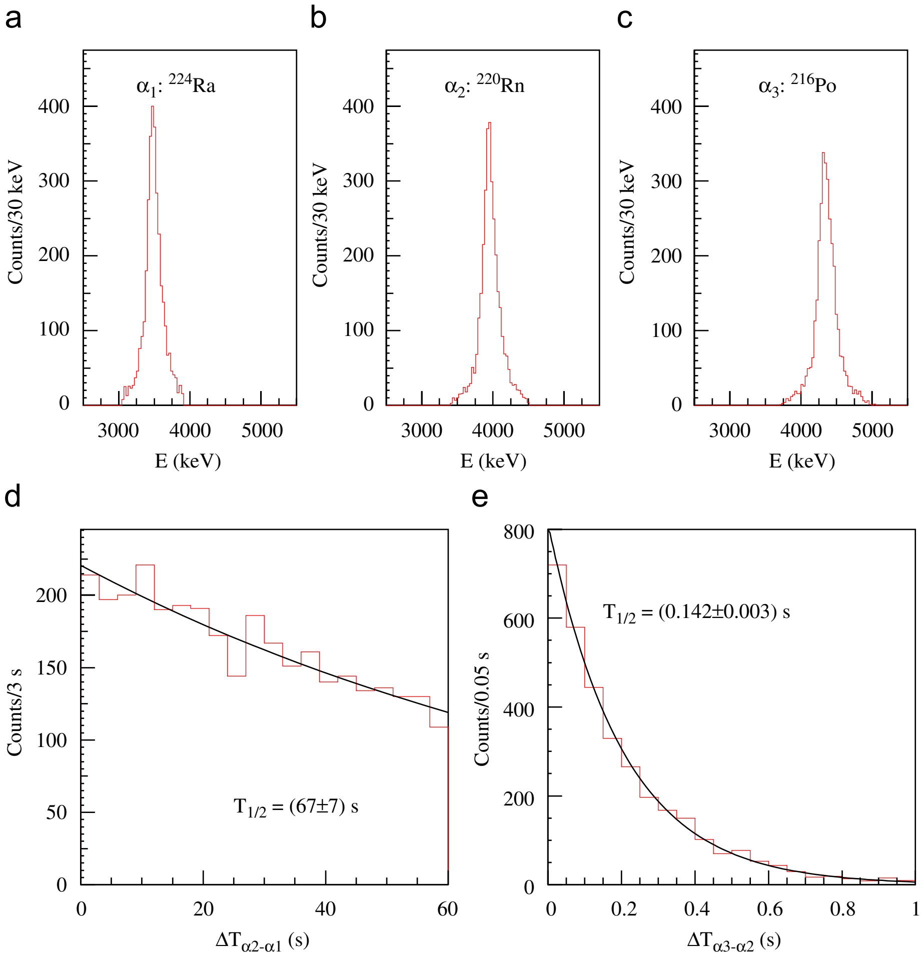

Fig. 7. *Top*: α peaks of ^{224}Ra, ^{220}Rn and ^{216}Po selected by the time–amplitude analysis (see text) from the data accumulated during an exposure of 8100 kg × day for the triple delayed coincidence with the detector (*d*) of Fig. 6. The energy resolutions (σ) are 75, 83, and 90 keV, well compatible with those expected by γ's calibrations (see Section 8). *Bottom*: Distributions of the time intervals between events due to ^{224}Ra and ^{220}Rn α decays (*left*) and between events due to ^{220}Rn and ^{216}Po α decays (*right*). The obtained half-lives of ^{220}Rn: 67 ± 7 s, and of ^{216}Po: 0.142 ± 0.003 s, are in agreement with the table values (55.6 and 0.145 s, respectively [25]).

^{220}Rn($Q_\alpha = 6.405$ MeV, $T_{1/2} = 55.6$ s) $\rightarrow$ ^{216}Po($Q_\alpha = 6.906$ MeV, $T_{1/2} = 0.145$ s) $\rightarrow$ ^{212}Pb.

An example of the obtained results for the detector (*d*) of Fig. 6 is shown in Fig. 7. The subchain has been selected by looking for events in the energy window 3050–3900 keV, followed within 60 s by another event in the energy window 3400–4500 keV, still followed within 1 s by the last event in the energy window 3650–5100 keV.

The α peaks as well as the distributions of the time intervals between the events are in a good agreement with those expected for the α's from the ^{224}Ra $\rightarrow$ ^{220}Rn $\rightarrow$ ^{216}Po $\rightarrow$ ^{212}Pb chain.

Moreover, the position of the α peaks, reported on an energy scale calibrated with γ sources, allows the determinination of the α/β light ratio in the used crystal; it is: $\alpha/\beta = 0.467(6) + 0.0257(10) \times E_\alpha$[MeV], where E_α[MeV] is the energy of the α particle in MeV.

The number of the triple delayed coincidences, selected by the given procedure, is 3310 in an exposure of 8100 kg × day. It corresponds, after applying the efficiencies, to $9.0 \pm 0.4\,\mu$Bq/kg.

Repeating the same analysis for all the crystals of the DAMA/LIBRA apparatus we obtain a ^{228}Th activity ranging from 2 to about 30 μBq/kg depending on the crystal.

For completeness we note that the activity value determined in this way for each detector is well consistent with that obtained in an independent analysis of the so-called Bi–Po events. The Bi–Po events are due to the ^{212}Bi β decay to ^{212}Po and to the subsequent ^{212}Po α ($Q_\alpha = 8.954$ MeV) decay to ^{208}Pb with $T_{1/2} = 299$ ns.[4] They can be clearly identified by the recorded pulse shapes over a 2048 ns time window. In particular, for the detector (*d*) of Fig. 6 the inferred activity for ^{228}Th decay subchain is $9.4 \pm 1.5\,\mu$Bq/kg, well compatible with the previous determination.

If the whole ^{232}Th radioactive chain is assumed at equilibrium (as it can be the case considering that the longest half-life of the daughter isotopes, ^{228}Ra, is 5.75 years), the ^{232}Th contents in the crystals typically range from 0.5 to 7.5 ppt.

5.2. ^{238}U

An estimate of the ^{238}U contamination can be obtained for each detector from the measured α activity and the ^{232}Th content evaluated above. Assuming—as a first approximation—that also the ^{238}U chain is in equilibrium, one obtains values ranging from 0.7 to 10 ppt depending on the crystal.

---

[4] Also the ^{238}U radioactive chain produces Bi-Po events, due to ^{214}Bi β decay to ^{214}Po and to the subsequent ^{214}Po α ($Q_\alpha = 7.833$ MeV) decay to ^{210}Pb with $T_{1/2} = 164.3\,\mu$s. In particular, their rate is connected with the activity of the ^{226}Ra $\rightarrow$ ^{210}Pb decay chain segment.

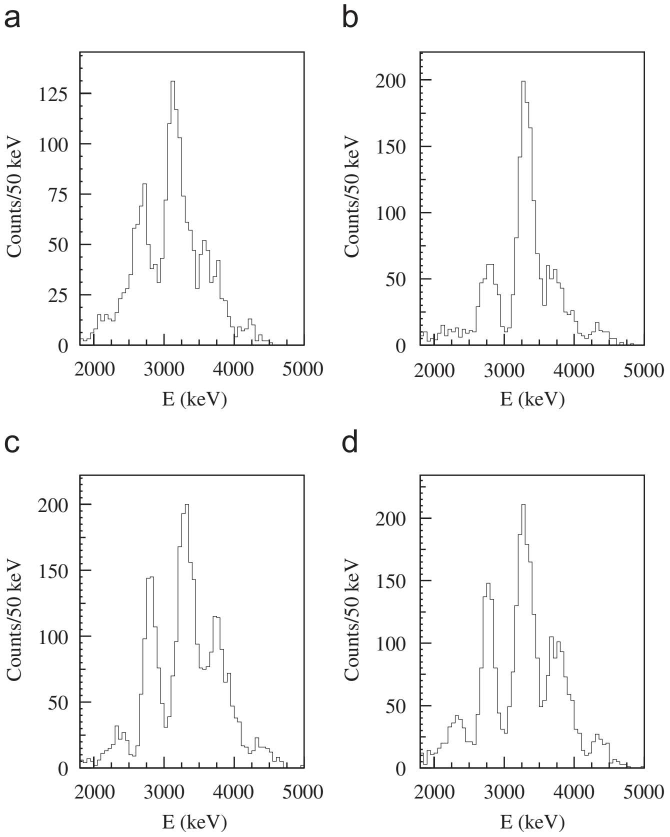

Fig. 8. The α energy distributions in some of the NaI(Tl) crystals corresponding to a live time of 570 h. The energy is given in keV electron equivalent.

However, the hypothesis of equilibrium for the ^{238}U chain in the detectors is not confirmed by the study of the energy distributions of the α particles, which can allow in principle the determination of the various contributions from the ^{238}U subchains. In Fig. 8, we show—as an example—the distributions of α from ^{238}U and ^{232}Th chains in some of the new NaI(Tl) crystals as collected in a live time of 570 h; there the α energies are given in keV electron equivalent.

In particular, starting from the low energy peak, the five α peaks in the energy spectra of Fig. 8 can be associated with[5]: (i) ^{232}Th ($Q_\alpha = 4.08$ MeV) + ^{238}U (4.27 MeV); (ii) ^{234}U (4.86 MeV) + ^{230}Th (4.77 MeV) + ^{226}Ra (4.87 MeV); (iii) ^{210}Po (5.41 MeV) + ^{228}Th (5.52 MeV) + ^{222}Rn (5.59 MeV) + ^{224}Ra (5.79 MeV); (iv) ^{218}Po (6.12 MeV) + ^{212}Bi (6.21 MeV) + ^{220}Rn (6.41 MeV) and (v) ^{216}Po (6.91 MeV). Thus, the contribution of each α decay has been simulated and fitted to the experimental energy spectra (some examples are given in Fig. 8) considering the ^{238}U radioactive chain split into five segments ($^{238}\text{U} \rightarrow {}^{234}\text{U} \rightarrow {}^{230}\text{Th} \rightarrow {}^{226}\text{Ra} \rightarrow {}^{210}\text{Pb} \rightarrow {}^{206}\text{Pb}$) and the ^{232}Th chain at equilibrium.

The fit of the measured alpha spectra allows the determination of the activities of the five ^{238}U subchains and of the ^{232}Th chain. The results confirm the hypotheses that the ^{238}U chain is broken in these NaI(Tl) crystals. As an example in the detector (*d*) of Figs. 6 and 8 the ^{232}Th and ^{238}U contents obtained by the fit are: (1) $8.5 \pm 0.5\,\mu$Bq/kg of ^{232}Th (that is, 2.1 ± 0.1 ppt, value in agreement with the two determinations given above using the time–amplitude and the Bi–Po analyses); (2) $4.4 \pm 0.7\,\mu$Bq/kg for $^{238}\text{U} \rightarrow {}^{234}\text{U}$ decay subchain (that is, 0.35 ± 0.06 ppt of ^{238}U); (3) $15.8 \pm 1.6\,\mu$Bq/kg for $^{234}\text{U} \rightarrow {}^{230}\text{Th} + {}^{230}\text{Th} \rightarrow {}^{226}\text{Ra}$ decay subchains (they all contribute to the same peak); (4) $21.7 \pm 1.1\,\mu$Bq/kg for $^{226}\text{Ra} \rightarrow {}^{210}\text{Pb}$ decay subchain and (5) $24.2 \pm 1.6\,\mu$Bq/kg for $^{210}\text{Pb} \rightarrow {}^{206}\text{Pb}$ decay subchain.

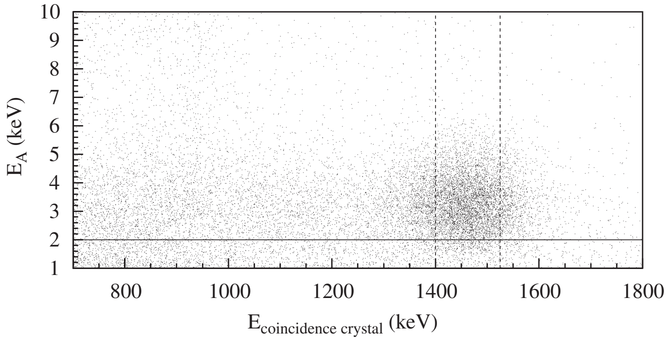

Fig. 9. Example of the analysis to determine $^{\text{nat}}$K contamination in one of the 25 crystals (see text). The scatter plot shows the low energy region of the considered crystal, A, as a function of the energy detected in the other crystal involved in the double coincidence. The threshold of each PMT is at single photoelectron level. For comparison, the software energy threshold used in the data analyses of the *single-hit* events for Dark Matter particle investigation: 2 keV, is shown as continuous line.

As it is clear e.g. from Fig. 8, the residual contaminants may be slightly different even among detectors made from NaI(Tl) crystals grown with the same selection of materials, purification processes and protocols. In fact, some casual pollutions during the growth and handling procedures may in principle be possible, being the detectors built in an industrial environment. Differences may also arise depending on the use of different bulks or on which part of a crystallized bulk has been used to build the detector. In fact, the purification during crystallization may be not uniform in the whole bulk mass. Moreover, the uniformity of the contaminants distribution inside the total material needed to construct each part of the detectors cannot be assured. Obviously, casual pollution may also occur when handling the detectors in industrial environment or deep underground without the needed extreme care.

5.3. ^{nat}K

An estimate of the potassium content in the DAMA/LIBRA crystals has been obtained investigating over large exposure the presence of peculiar double coincidences. In fact, the ^{40}K (0.0117% of $^{\text{nat}}$K) also decays by EC to the 1461 keV level of ^{40}Ar (b.r. 10.66%) followed by X-rays/Auger electrons, that are contained in the crystal with efficiency ∼1, and a 1461 keV de-excitation γ. The latter one can escape from one detector (hereafter A) and hit another one, causing the double coincidence. The X-rays/Auger electrons give rise in the detector A to a 3.2 keV peak, binding energy of shell K in ^{40}Ar.[6]

The experimental data have been analyzed searching for these double coincidences; Fig. 9 shows as an example a scatter plot of the energies of the detector A and all the other detectors involved in the coincidence. It is evident a spot that correlates the 1461 keV events in the other crystals with the 3.2 keV peak in crystal A. The detection efficiency for such coincidences has been evaluated for each crystal by Monte-Carlo code. The analysis has given for the $^{\text{nat}}$K content in the crystals values not exceeding about 20 ppb. It is worth noting that the identification of the 3.2 keV peak offers also

---

[5] It is worth noting that the α associated with the decays of ^{212}Po and of ^{214}Po are not present in the shown α plots because they belong to a Bi–Po event and they are mainly vetoed by the acquisition system (see later).

[6] In the $76.3 \pm 0.2\%$ of the cases an electron from shell K ($E_K = 3.2$ keV) is involved in the process, in the $20.9 \pm 0.1\%$ an electron from shell L ($E_L = 0.3$ keV) and in $2.74 \pm 0.02\%$ electron from upper shells.

an intrinsic calibration of each DAMA/LIBRA detector in the lowest energy region (see Section 8).

5.4. ^{125}I

As regards possible non-standard contaminants, we remind that during the period of powders' storage and/or crystal growing and handling at sea level (of order of at least some months for large crystals) radioactive isotopes can be produced by cosmic-ray interactions. Therefore, it is good practice in this kind of experiments to wait for the decay of the short-life cosmogenic isotopes before considering the production data in underground.

In particular, here we comment the case of cosmogenic ^{125}I which decays by EC to ^{125}Te giving 35.5 keV γ's (or internal conversion electrons) and, at the same time, tellurium X-rays and Auger electrons, whose total energy is 31.8 keV, giving rise to a peak around $\simeq$ 67 keV with half-life 59.40 days (see Fig. 10). In this case, the best situation is reached after $\simeq$ 8 months of storage deep underground.

Some arguments on cosmogenic activation in NaI(Tl) can be found in Ref. [26], while the production rate of cosmogenic isotopes can be calculated mainly according to the model of Ref. [27]. However, the activity of cosmogenic isotopes in NaI(Tl) detectors would be in practice generally lower than the calculated one because of purification and saturation processes during the growing procedures.

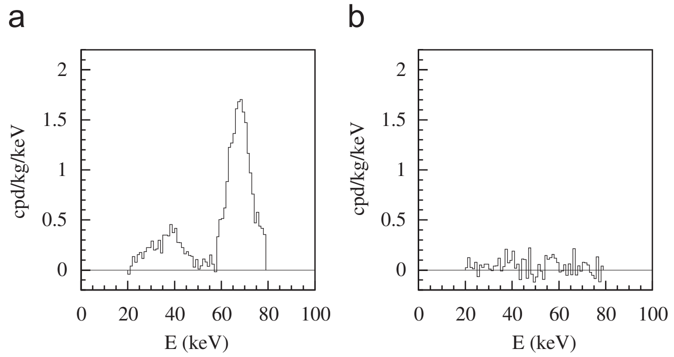

Fig. 10. (a) Difference between the energy distributions collected at Gran Sasso with a DAMA/LIBRA NaI(Tl) detector just stored underground and 15 months later. The role of $\simeq$ 67 keV peak due to ^{125}I activation (half-life 59.40 days) is evident. In particular, the EC of ^{125}I from shell K (80.12%) gives rise to the 67.3 keV peak, while EC from upper shells produces the $\simeq$ 40 keV peak. (b) The same as (a) but obtained for a detector stored underground for a longer time; the peaks due to ^{125}I are not present.

5.5. ^{129}I and ^{210}Pb

The cosmogenic ^{129}I ($T_{1/2} = 1.57 \times 10^7$ yr) can be present in the natural Iodine with a percentage of the order of 1.5×10^{-12} (considering sediments below the zone of bioturbation, i.e. without the presence of anthropogenic Iodine [28]). It decays by β^- into the excited level of ^{129}Xe at 39.57 keV. Thus, this process produces a de-excitation γ of 39.57 keV (or internal conversion electron) plus an electron with energy distribution according to the beta spectrum of ^{129}I (maximum energy 154 keV). Therefore, the total energy deposited in the crystal from this process has a peculiar distribution with sharp rise around $\simeq$ 40 keV and smooth behaviour up to $\simeq$ 194 keV (sum of the gamma energy and of the maximum energy of the electrons). Fig. 11 shows the energy spectra of two detectors in the energy region of interest for this process and the model of background. Hence, the amount of cosmogenic ^{129}I has been estimated to be there $^{129}\mathrm{I}/^{\mathrm{nat}}\mathrm{I} = (1.7 \pm 0.1) \times 10^{-13}$. If this value is used for dating the NaI powders, one obtains that they have been extracted from an ore with an age of order of 50 Myr.

Fig. 11 also allows an independent evaluation of the content of ^{210}Pb in the crystals. The ^{210}Pb isotope β decays with a branching ratio of 84% into the excited level of ^{210}Bi at 46.5 keV; the electron has an energy distribution according to the beta spectrum (maximum energy: 16.6 keV). The presence of a contamination of ^{210}Pb mainly on the housings' surfaces has been used by the DAMA/NaI apparatus as a calibration point at 46.5 keV (due to the gamma from the de-excitation of the ^{210}Bi excited level) during its data taking (see for example, Refs. [2,4]). Such a peak is not so appreciable in the new DAMA/LIBRA detectors; anyhow, the contents of internal ^{210}Pb can be determined for these detectors by investigating the energy region around $\simeq$ 50 keV. For the two detectors of Fig. 11 one gets $7 \pm 4\,\mu$Bq/kg (safely corresponding to an upper limit of $<12\,\mu$Bq/kg at 90% C.L.) and $29 \pm 3\,\mu$Bq/kg, respectively. Let us note that for the second detector in Fig. 11—corresponding to the detector (*d*) of Figs. 6 and 8—an independent determination of ^{210}Pb content has been mentioned above when studying the α spectrum in the crystals: the two values are well compatible.

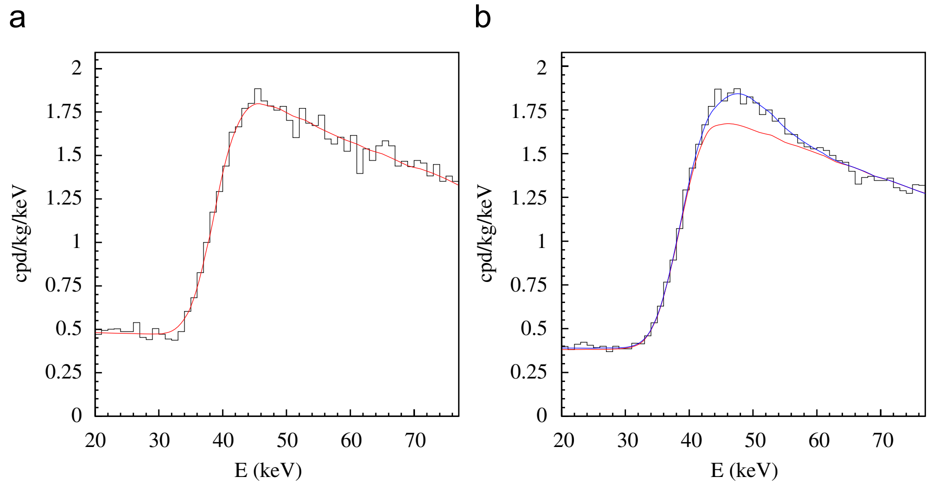

Fig. 11. Energy distributions of two new DAMA/LIBRA NaI(Tl) detectors in the energy region of interest for the cosmogenic ^{129}I decay process (histogram) and the model of background (lines). The contribution of internal ^{210}Pb is visible only in the plot of the second crystal ($<12\,\mu$Bq/kg at 90% C.L. and $29 \pm 3\,\mu$Bq/kg, respectively). The amount of cosmogenic ^{129}I has been estimated to be $^{129}\mathrm{I}/^{\mathrm{nat}}\mathrm{I} = (1.7 \pm 0.1) \times 10^{-13}$ for both the crystals.

Repeating the same analysis for all the new DAMA/LIBRA detectors, we obtain that the amount of cosmogenic ^{129}I is at the same level for all the new DAMA/LIBRA detectors; in addition, the content of ^{210}Pb in the crystals typically ranges: $5-30\,\mu$Bq/kg.

5.6. ^{22}Na

Among the possible isotopes produced by cosmogenic activation at sea level in NaI(Tl) we also investigate the ^{22}Na ($T_{1/2} = 2.6$ yr). The calculated maximum rate level is $\simeq 100$ cpd/kg at sea level. An estimate of the ^{22}Na activity in the detectors can be obtained by searching for triple coincidences induced by the β^+ decay of ^{22}Na followed by 1274.6 keV de-excitation γ (b.r. 90.33%). In particular, we have searched for events where the positron and one of the two 511 keV annihilation γ release all their energy in one detector while the second 511 keV annihilation γ and the 1274.6 keV γ hit other two detectors. For example, choosing an energy window of 650–1000 keV for the first detector and $\pm 2\sigma$ around 511 keV for the second one, we look for the typical peak at 1274.6 keV in the third detector. Accounting for the detection efficiency of the process, the obtained activity in the detectors ranges from an upper limit of $15\,\mu$Bq/kg (90% C.L.) to some tens μBq/kg depending on their arrival time underground.

5.7. ^{24}Na

Another source of internal background is the possible presence of ^{24}Na.

In fact, environmental neutrons would induce the reaction ^{23}Na(n, γ)^{24}Na with 0.1 barn cross-section and the reaction ^{23}Na(n, γ)$^{24\mathrm{m}}$Na with 0.43 barn cross-section [29]. The ^{24}Na isotope is a β-emitter (end point equal to 1.391 MeV) with two prompt associated γ's (2.754 and 1.369 MeV). On the other hand, the $^{24\mathrm{m}}$Na isotope decays 100% of the times in ^{24}Na by internal transition with a γ of 0.472 MeV. Thus, the presence of ^{24}Na has been investigated with high sensitivity by looking for triple coincidences induced by a β (E1) in one detector and the two γ's in two adjacent ones (E2, E3). In particular, we consider: (i) $0.57\,\mathrm{MeV} < \mathrm{E1} < 1.3\,\mathrm{MeV}$, (ii) E2 and E3 inside $\pm 1\sigma$ energy windows around the photopeak positions. Only one event satisfying the requirements has been found in the considered data set (106 376 kg × day); it can also be ascribed to side processes (for example to the decay of ^{208}Tl in the ^{232}Th chain). Safely, we consider that the number of detected events is lower than 3.89 (90% C.L.) following the procedure given in Ref. [30]; thus, accounting for the detection efficiency of the process, an upper limit of 2409 ^{24}Na decays (90% C.L.) is obtained for the considered exposure. It corresponds to an activity $< 0.26\,\mu$Bq/kg (90% C.L.). Assuming the production of these short-life isotopes as fully due to a steady thermal neutron flux, an upper limit on the thermal neutron flux surviving the multicomponent DAMA/LIBRA shield can be derived as $< 1.2 \times 10^{-7}\,\mathrm{cm}^{-2}\,\mathrm{s}^{-1}$ (90% C.L.).

5.8. Miscellanea

Finally, as regards the ^{3}H ($T_{1/2} = 12.3$ yr),[7] the calculated maximum rate is $\simeq 20$ cpd/kg at sea level. However, as mentioned above, in real conditions the ^{3}H activity in a NaI(Tl) detector would be essentially lower than the calculated maximum level, because it would be extracted in the process of NaI(Tl) purification and growth. In our crystals the ^{3}H content has been estimated to be $< 0.9 \times 10^{-4}$ Bq/kg at 95% C.L. Moreover, for the ^{87}Rb ($T_{1/2} = 4.8 \times 10^{10}$ yr), and for the ^{85}Kr ($T_{1/2} = 10.7$ yr) isotopes we just mention the obtained upper limits (95% C.L.): $< 3 \times 10^{-4}$ Bq/kg and $< 10^{-5}$ Bq/kg, respectively.

6. The photomultipliers

The photomultipliers used in this experiment have been built by Electron Tubes Limited and longly stored underground. The PMTs are made of ultra-low background glass. The materials entering in the construction of the PMT have been selected by various kind of measurements and, in particular, measurements on samples have also been carried out with low background DAMA/Ge detector deep underground.

The PMTs have flying leads (instead of a hard socket) and are directly connected to suitable voltage dividers (see Fig. 12). The voltage dividers have been assembled deep underground with miniaturized SMD resistors and capacitors (also selected for radiopurity by low background Ge detector) and mounted on thin teflon sockets (see Fig. 12). All the solders were performed by using low radioactive Boliden lead and low radioactive resin.

The voltage dividers have been optimized to reach the best signal/noise ratio; a scheme is shown in Fig. 13.

The applied high voltage is positive; in this way the cathode is maintained to ground in order to avoid any voltage difference with the PMT window, light guide and the copper housing.

The PMTs work near the maximum high voltage—within the linearity plateau—in order to assure a suitable energy threshold and to improve the PMT noise rejection near it.

The PMTs have nine high gain, high stability dynodes of linear focused design, high quantum efficiency ($\simeq 30\%$ at 380 nm), good pulse height resolution for single photoelectron pulses (peak/valley $\gtrsim 2$), low dark noise rate ($\simeq 0.1$ kHz), and a gain of $\simeq 10^6$. In the experiment each detector has two PMTs both to increase the light collection and to reduce the PMT noise contribution near energy threshold. They work in coincidence at single photoelectron threshold.

The residual contaminants in the PMTs have been measured with and without a bent light guide (i.e. shielding and not shielding the PMT contribution) and a low background NaI(Tl); typically ^{232}Th and ^{238}U are lower than few tens ppb and $^{\mathrm{nat}}$K is of order of few tens ppm. The PMT contribution to the counting rate is further reduced by using 3 in. diameter 10 cm long UV light

Fig. 12. *Left*: A DAMA/LIBRA PMT with flying leads directly connected to the voltage divider. *Right*: A voltage divider assembled with miniaturized SMD resistors and capacitors mounted in thin teflon socket.

---

[7] The ^{3}H can be produced by spallation processes induced by cosmic rays on ^{23}Na and ^{127}I. In particular, we recall $n + {}^{23}\mathrm{Na} \rightarrow {}^{3}\mathrm{H} + {}^{21}\mathrm{Ne}$ (stable) and $n + {}^{127}\mathrm{I} \rightarrow {}^{3}\mathrm{H} + {}^{125}\mathrm{Te}$ (stable), for neutron with energy $\gtrsim 15, 20$ MeV.

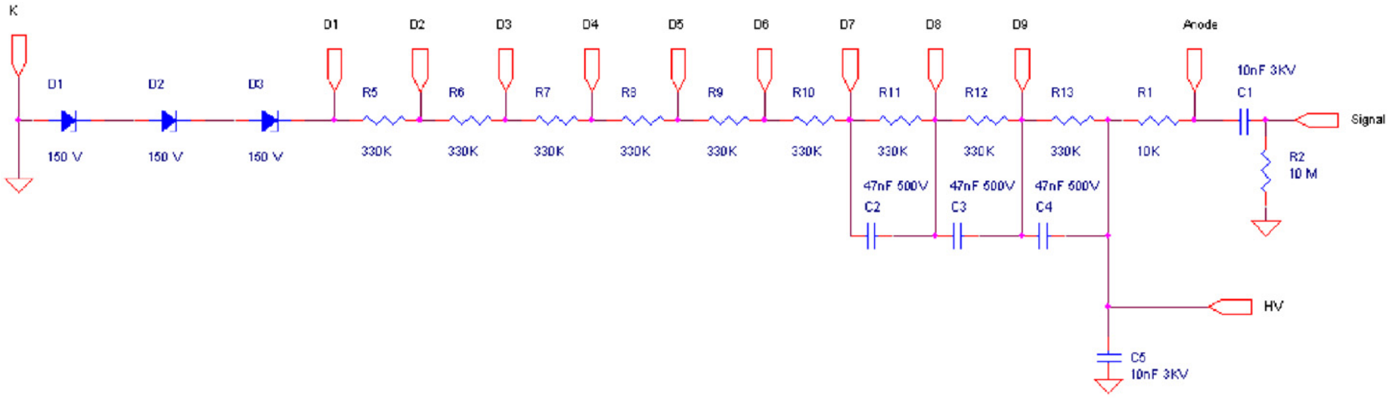

Fig. 13. The voltage divider scheme.

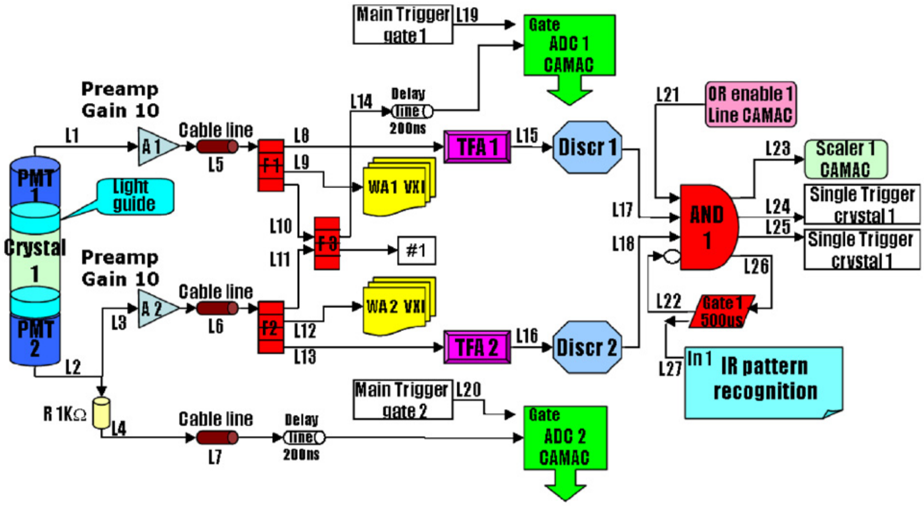

Fig. 14. The conceptual scheme of the electronic devices of a single detector. Devices processing analog signals and those providing the trigger of the single detector are shown.

guides (made of Suprasil B) which also act as optical windows, as mentioned above. The highly radiopure light guides assure both suitable low radioactivity (<1 ppb of ^{238}U, <2 ppb of ^{232}Th, and <1.3 ppm of ^{nat}K as measured by Ge detectors) and very suitable optical characteristics for the NaI(Tl) light emission, being transparent down to 300 nm.

Finally, to further reduce the PMTs contribution to the background, in the DAMA/LIBRA apparatus each PMT and related light guide are surrounded by a shaped low-radioactivity copper shield (see Section 4 and Fig. 4(b)).

7. The electronic chain

Each crystal of the DAMA/LIBRA apparatus is viewed by two PMTs with grounded cathode and supplied by positive high voltage. The HV power supply for the PMTs is given by a CAEN multichannel voltage supply with voltage stability of 0.1%.

Fig. 14 shows the scheme of the electronic devices of a single detector. In particular, the part of the chain regarding the analog signals and their processing are shown. It is also reported the logic devices providing the trigger of the single detector. The signals from each PMT are amplified by a preamplifier having 0–250 MHz bandwidth, a factor 10 gain and a voltage integral linearity ±0.2%.

The signal from PMT 2 (see Fig. 14) is divided in two branches by a resistive passive splitter: 19/20 of the signal is sent to the preamplifier, while the remaining 1/20—suitably delayed—feeds the CAMAC charge ADC 2 (QADC *high energy*) unit. This latter allows the process of the high energy pulses, which instead saturate the remaining part of the electronics. The preamplified signals of PMT 1 and PMT 2 are the inputs of linear Fan-in/Fan-out devices F1 and F2. They produce three copies of each signal: (i) the first copies of PMT 1 and PMT 2 signals are sent to two separate channels of a Waveform Analyzer, which records the signals in a time window of 2048 ns. This is accomplished by using fast VXI Tektronix four-channel TVS641A digitizers with a sampling frequency of 1 GSample/s and 250 MHz bandwidth; (ii) the second copies of PMT 1 and PMT 2 signals are added and sent to the input—after a delay line—of the CAMAC charge ADC 1 (QADC *low energy*) and to a Spectroscopy Amplifier (#1, see later); (iii) the last copies are used to generate the trigger of the crystal. These latter ones are shaped by Timing Filter Amplifiers (TFA1 and TFA2) with an integration time of 50 ns; their outputs are discriminated by DISCR1 and DISCR2 with the thresholds at the single photoelectron level. The coincidence (AND 1) between the two logical NIM outputs provides the trigger of the considered detector.

In order to reject afterglows, Cherenkov pulses in the light guides and Bi-Po events, a 500 μs veto occurs after each event selected by the coincidence (Gate 1 in Fig. 14); this veto introduces a negligible systematic error on the measured rate ($\lesssim 10^{-4}$).

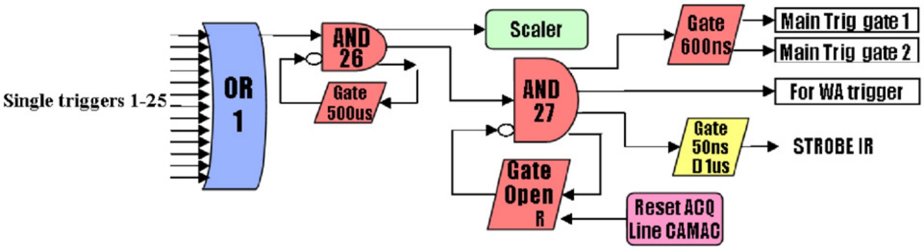

Fig. 15. The conceptual scheme of the electronic chain providing the main trigger of DAQ.

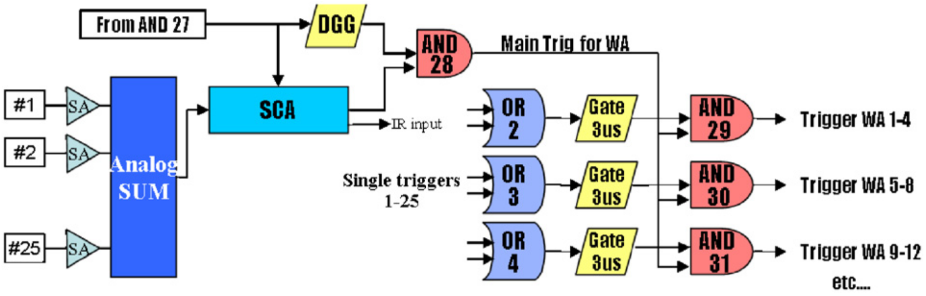

Fig. 16. The conceptual scheme of the logic system managing the individual triggers of the Waveform Analyzers.

A CAMAC Output Register (OR) provides the signal able to activate the coincidence module of each detector; this feature can be used, for example, during the calibration runs to enable the detector to be calibrated.

The outputs of the coincidence device (AND 1) provide: (i) the signal for a CAMAC scaler to count the number of triggers of each detector. The ratio of this number to the elapsed time gives the *hardware rate*, R_{Hj} of the *j*th detector; (ii) the line used in the main trigger electronic chain (see later and Fig. 15); (iii) the line used in the logic system managing the individual triggers of the Waveform Analyzers (see later and Fig. 16); (iv) the line giving the start to the Gate 1 which—in addition to the veto of the coincidence AND 1—feeds a CAMAC I/R Pattern Recognition (IR). The IR allows the identification of the detector/detectors involved in the main trigger.

The electronic devices which generate the main trigger of the acquisition are shown in Fig. 15. The main trigger is provided by the logic OR (OR 1) of all the crystals. The main trigger NIM logic pulses are counted by a Scaler. Devoted devices manage the trigger only when the acquisition is ready (see Fig. 15); they issue the trigger of the DAQ. The dead time of the acquisition is properly evaluated by using the information from the Scaler. The live time is estimated straightforward.

When a DAQ trigger occurs, the following logic signals are issued to: (i) the Gate Generator producing the 600 ns gates for the charge ADCs (QADC); (ii) the Delay Gate Generator giving the strobe signal to the CAMAC I/R Pattern Recognition. This device also generates the LAM in the CAMAC system, and, therefore, the interrupt to the CPU of the acquisition computer; (iii) the logic system managing the individual triggers of the Waveform Analyzers.

The logic system of the individual triggers of the Waveform Analyzers has been introduced in order to speed up the DAQ. In particular, the trigger of the Waveform Analyzers (see Fig. 16) are issued only if the total energy deposited in the detectors is in an energy window suitably chosen. For this purpose, each line feeds a Spectroscopy Amplifier (SA) whose gain is equalized. The analog sum of the SA signals of all the detectors, whose stability is monitored by a peak ADC (not shown in the scheme), feeds a Single Channel Analyzer (SCA) which allows the selection just of events in the chosen energy window. A devoted electronic circuit issues the trigger of the Waveform Analyzers[8] allocating the detectors producing the main trigger. Summarizing, an individual trigger to a given Waveform Analyzer is issued when the following three conditions are fulfilled: (i) at least one of its corresponding lines has fired; (ii) the DAQ trigger is present; (iii) the total energy of the events is in the chosen energy window. Let us remind that for the events with energy outside the chosen energy window (e.g. high energy events) the QADC values are acquired anyhow.

The data acquisition system is made of a Workstation by Compaq with Linux Operating System, interfaced with the hardware system through MXI-2 and GPIB buses (see Fig. 17). The GPIB bus allows the communication with the CAMAC crate housing the QADCs, the scalers and the I/O registers, while the MXI-2 bus allows to communicate with the three VXI mainframes, where the Waveform Analyzers are installed.

The information collected by DAQ, when a DAQ trigger occurs, are: (i) the time of occurrence of the event; (ii) the pattern of the detectors firing; (iii) for each fired detector the QADC channels and the pulse profiles of the two PMTs of the detector as recorded by the Waveform Analyzer, when the conditions given above are fulfilled. In particular, the areas of the pulse profiles (*TD channel*) are proportional to the energy released in the detector (see Section 8). Other variables can be constructed by the pulse profiles and they can be used for noise rejection (see Section 8). For high energy events the energy can be estimated in terms of QADC channels (see Section 8).

Moreover, let us remind that the DAQ also records—together with the production data—the information coming from the monitoring system, as mentioned above (also see Fig. 3).

In near future, the DAMA/LIBRA DAQ will be improved and new Waveform Analyzers will be introduced. In particular, in the new

---

[8] We remind that each Waveform Analyzer has four channels and, therefore, allocates the signals of two detectors.

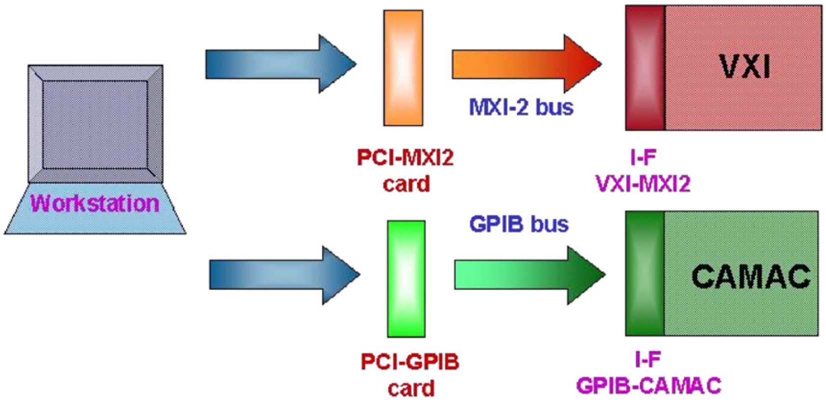

Fig. 17. Data acquisition system of DAMA/LIBRA.

DAQ a HP Workstation with Intel processor (3.4 GHz) and Red-Hat Linux Operating System will be interfaced with the hardware system through MXI-3 and GPIB buses. The new MXI-3 bus will communicate with the new Waveform Analyzers through a CompactPCI mainframe. The new Waveform Analyzers will be Quad-Channel CompactPCI Digitizer Acqiris DC270 with 250 MHz bandwidth and a sampling frequency of 1 GSample/s simultaneously on all four channels. The data will be transferred on fiber optics from the Waveform Analyzers to PC (electrically decoupled).

8. General features

8.1. Uniformity of the light collection

The absence of dead spaces in the light collection has been carefully investigated by performing suitable calibrations in different positions of the detector; in fact, by irradiating the whole detector with high-energy γ sources (e.g., ^{137}Cs) from different positions, no significant variations of the peak position and energy resolution have been observed. Moreover, the α peaks at high energy (see Fig. 7) and their energy resolutions are well compatible with those expected for γ calibration (see above) and also support the uniformity of the light collection within 0.5%.[9]

8.2. Photoelectrons/keV

The number of photoelectrons/keV has been derived for each detector from the information collected by the Waveform Analyzer over its large time window (2048 ns).

In fact, a clean sample of photoelectrons can be extracted from the end part of this time window; there the scintillation pulses are completely ended, while afterglow single photoelectron signals can be present. As an example, Fig. 18 shows a typical experimental distribution of the area of the single photoelectron's pulses for a DAMA/LIBRA detector. The relative peak value can be compared with the peak position of the distribution of the areas of the pulses corresponding to a full energy deposition from the 59.5 keV of the ^{241}Am source. This procedure permits to obtain the number of photoelectrons/keV searched for; they ranges from 5.5 to 7.5 photoelectrons/keV depending on the detector.

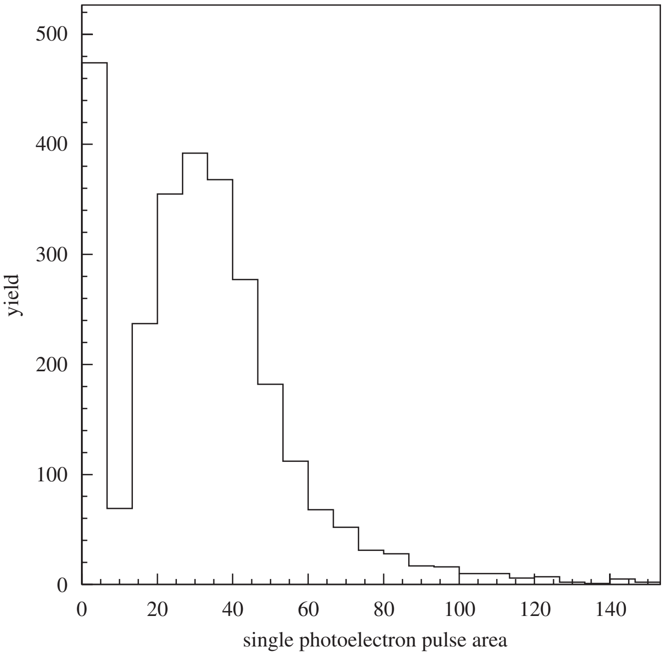

Fig. 18. Typical experimental distribution of the area of the single photoelectron's pulses for a DAMA/LIBRA detector, as recorded by the Waveform Analyzer over 2048 ns time window. From this picture 6.7 photoelectrons/keV have been inferred for this detector.

8.3. Calibrations at low and high energy

The low (up to ~100 keV) and the high (above ~100 keV) energy regions have been studied by using various external gamma sources and internal X-rays or gamma's. In particular, as shown in Fig. 19, gammas from ^{241}Am and from ^{133}Ba external sources provide 30.4 keV (composite), 59.5 keV and 81.0 keV peaks; moreover, other calibration points can be obtained by: (i) the internal X-rays at 3.2 keV (see Figs. 9 and 19); (ii) the gammas and/or X-rays and/or Auger electrons due to internal ^{125}I (see Figs. 10(a) and 19), giving two structures in the energy spectrum at 40.4 keV (composite peak) and at 67.3 keV; (iii) the gammas at 39.6 keV plus the β spectrum due to cosmogenic ^{129}I (see Fig. 11).

---

[9] For example, from Fig. 7(a) the energy resolution is $\sigma = 75 \pm 3$ keV, while the expected one from the fit of Fig. 22 is 72 keV. Hence, with the help of a simulation of the light collection, an upper limit of about 0.5% can be set on the disuniformity of the light collection.

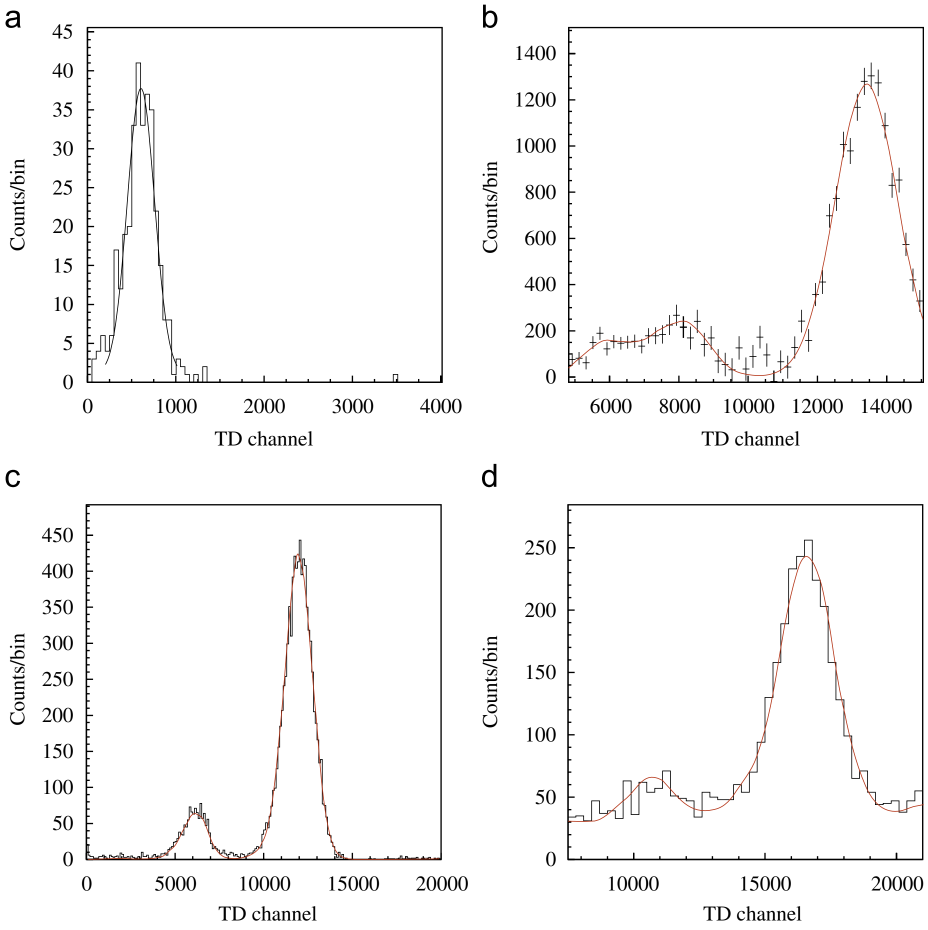

Fig. 19. Examples of energy (pulse area) distributions for: (i) X-rays/Auger electrons (3.2 keV) due to internal ^{40}K (*top left*); (ii) gammas and/or X-rays and/or Auger electrons—mainly two structures in the energy spectrum at 40.4 keV (composite peak) and at 67.3 keV—due to internal ^{125}I (*top right*); (iii) gammas from ^{241}Am external source (*bottom left*); (iv) gammas of 81 keV from ^{133}Ba external source (*bottom right*). The lines superimposed to the experimental data have been obtained by Monte-Carlo simulations, obviously taking into account the geometry and all the involved materials.

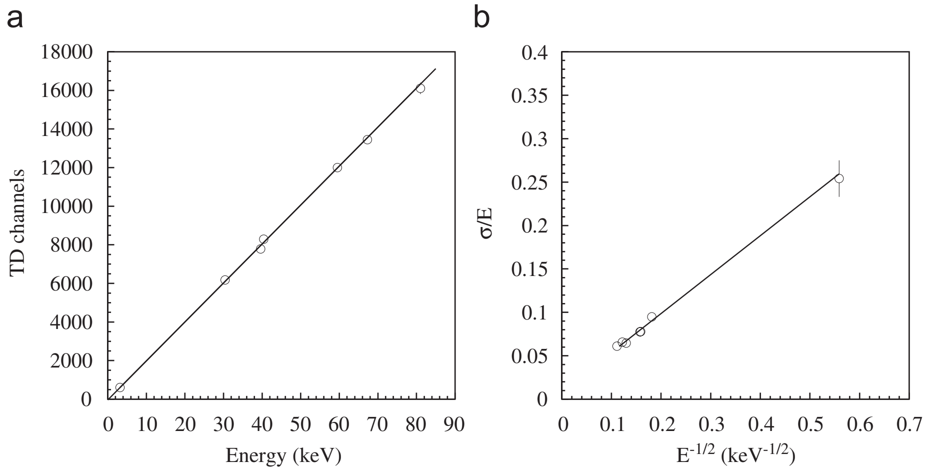

Fig. 20. Linearity of the pulse area as a function of the energy and energy resolution (σ/E) as a function of $E^{-1/2}$ for low energy calibrations (internal and external radiation).

In running conditions routine calibrations with ^{241}Am sources are regularly carried out.

The linearity of the pulse area as a function of the energy of the calibration points and the energy resolution in the low energy region are depicted in Fig. 20. The energy resolution behavior for the low energy scale has been fitted by a straight line: $\sigma_{\mathrm{LE}}/E = \alpha_{\mathrm{LE}}/\sqrt{E(\mathrm{keV})} + \beta_{\mathrm{LE}}$; the best fit values are $\alpha_{\mathrm{LE}} = 0.448 \pm 0.035$ and $\beta_{\mathrm{LE}} = (9.1 \pm 5.1) \times 10^{-3}$.

We remind here that, although the optimization is made for the lowest energy region, the data are taken on the full energy scale up to the MeV region by means QADCs. Thus, the high energy scale of the QADC has been calibrated mainly by using

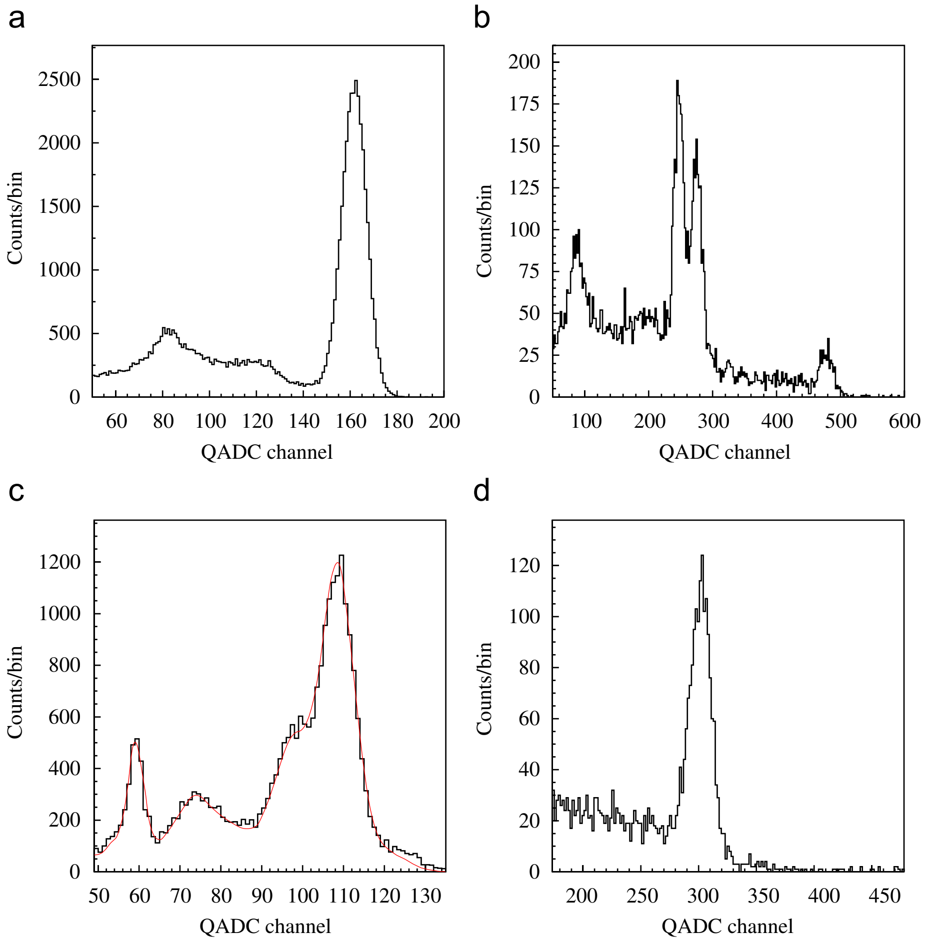

Fig. 21. Energy distributions for the external sources: ^{137}Cs, 662 keV γ rays (*top left*); ^{60}Co, 1173 and 1332 keV γ rays and their sum: 2505 keV (*top right*); ^{133}Ba, mainly 81 and 356 keV γ rays (*bottom left*). Energy distribution for γ rays of 1461 keV (*bottom right*) due to ^{40}K decays, tagged by the 3.2 keV X-rays in an adjacent detector (see also Fig. 9). The line superimposed to the experimental data of the ^{133}Ba spectrum has been obtained by Monte-Carlo simulations. Here in abscissa the QADC channel is reported.

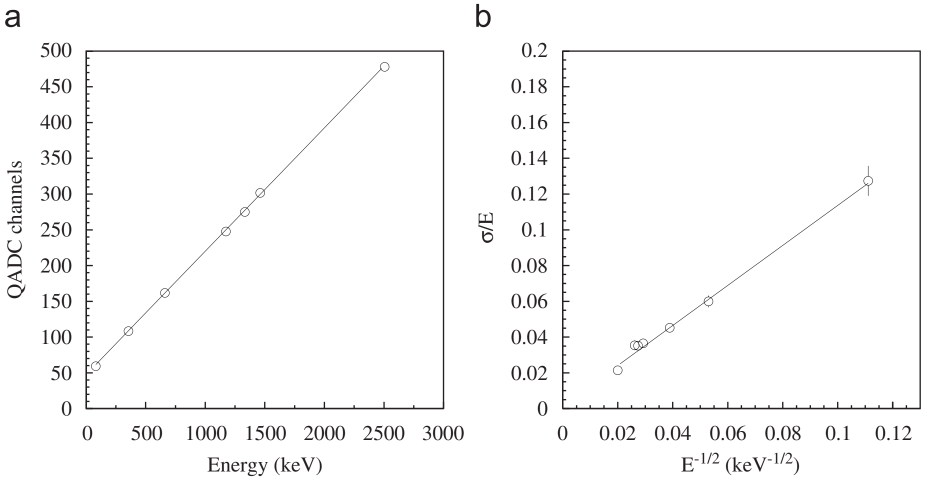

Fig. 22. Linearity of the QADC as a function of the energy and energy resolution (σ/E) as a function of $E^{-1/2}$ in the high energy region. We remind that the signals—unlike low energy events—for high energy events are taken only from one PMT.

external sources of γ rays, such as: ^{137}Cs (662 keV), ^{60}Co (1173 and 1332 keV and their sum: 2505 keV) and ^{133}Ba (mainly 81 and 356 keV); examples are reported in Fig. 21. Moreover, γ rays of 1461 keV due to ^{40}K decays, tagged by the 3.2 keV X-rays in an adjacent detector (see also Fig. 9), have been used.

The linearity of the QADC as a function of the energy and the energy resolution in the high energy region are reported in Fig. 22. The energy resolution behavior for the high energy scale has been fitted by a straight line: $\sigma_{\mathrm{HE}}/E = \frac{\alpha_{\mathrm{HE}}}{\sqrt{E(\mathrm{keV})}} + \beta_{\mathrm{HE}}$; the best fit values are $\alpha_{\mathrm{HE}} = 1.12 \pm 0.06$ and $\beta_{\mathrm{HE}} = (17 \pm 23) \times 10^{-4}$. The value α_{HE} is larger than the corresponding value at low energy since—as discussed previously—the signals for high energy events are taken only from one PMT.

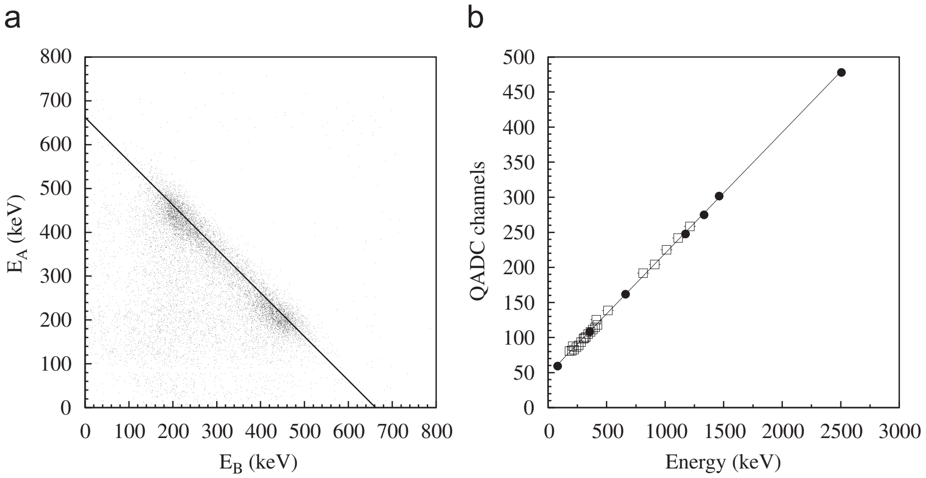

Fig. 23. *Left:* Example of a scatter plot of the energies, E_A and E_B, of two detectors A and B when using an external ^{137}Cs source placed in between. The solid line represents the case $E_A + E_B = 662$ keV, energy of the γ rays. The data points around this line correspond to events where the γ has a Compton back-scattering in one detector and the scattered γ is completely absorbed in the other one. *Right:* Linearity of the QADC as a function of the energy: data points from Fig. 22 (filled points) and from tagged γ's by double coincidences as described in the text (squared points).

Another method to study the linearity is to use events of double coincidences when two detectors are irradiated by γ's of known energy, E_γ. As an example, Fig. 23(*left*) shows the scatter plot of the energies, E_A and E_B, of the two detectors A and B when using an external ^{137}Cs source placed in between. The solid line represents the case $E_A + E_B = E_\gamma$; the data points around this line correspond to events where the 662 keV γ has a Compton back-scattering in one detector and the scattered γ is completely absorbed in the other one. Fixing a slice—for example at a fixed E_B value—it is possible to extract the peak position on the E_A variable. Applying this procedure to the high energy calibration data from various sources other points can be added in the linearity plot, as done in Fig. 23(*right*).

8.4. *Procedures for noise rejection near the energy threshold*

The only data treatment which is performed on the raw data is to eliminate obvious noise events (whose number sharply decreases when increasing the number of available photoelectrons) near the energy threshold. In particular, the DAMA/LIBRA detectors are seen by two PMTs working in coincidence and this already strongly reduces the noise near the energy threshold for the *single-hit* events (of interest for Dark Matter particles detection), while obviously noise is practically absent in *multiple-hit* events (see e.g. the double coincidence case of Fig. 9), since the probability to have random coincidences is negligible ($<3\times10^{-6}$).

Moreover, the NaI(Tl) is a suitable detector for an effective noise rejection, having no contribution from microphonic noise (as it is instead the case e.g. of ionizing and bolometer detectors) and being the physical pulses well distinguishable from the noise pulses, essentially PMT noise. This effectiveness is higher when a high number of photoelectrons/keV is available and when PMTs with suitable performances have been built, as in the present case.

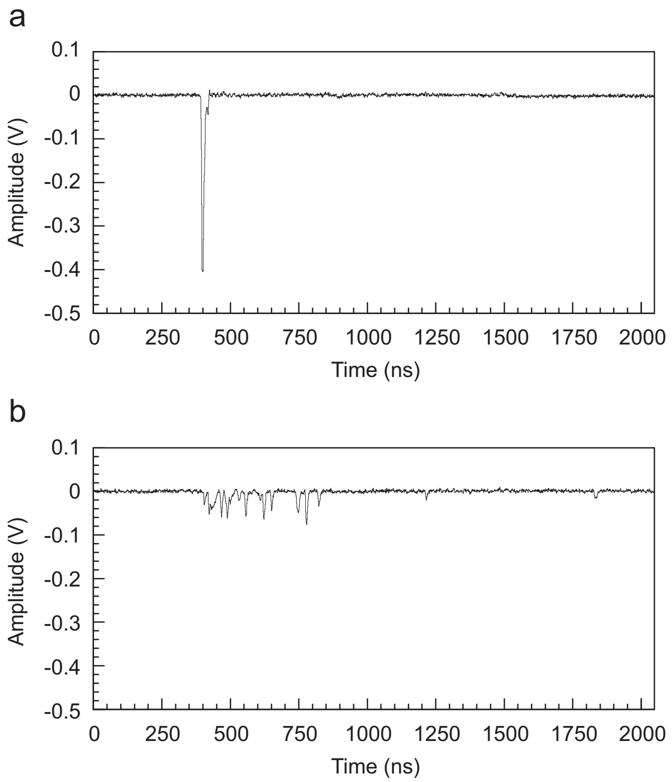

Fig. 24. Typical pulse profiles of PMT noise (*top*) and of scintillation event (*bottom*) with the same area, just above the energy threshold of 2 keV.

The noise rejection in the *single-hit* events is performed by considering that the scintillation pulses in NaI(Tl) have a time distribution with decay time of order of hundreds of ns (typically $\simeq 240$ ns), while the noise pulses are single fast photoelectrons pulses with decay time of order of tens of ns (see Fig. 24). The different time characteristics of these signals can be investigated building several variables from the information recorded for each pulse by the Waveform Analyser over the 2048 ns time window. The variables follow different distributions for scintillation and noise pulses. In particular, the fractions of the pulse areas evaluated over different time intervals, such as

$$X_1 = \frac{\text{Area (from 100 to 600 ns)}}{\text{Area (from 0 to 600 ns)}};\qquad X_2 = \frac{\text{Area (from 0 to 50 ns)}}{\text{Area (from 0 to 600 ns)}} \tag{1}$$

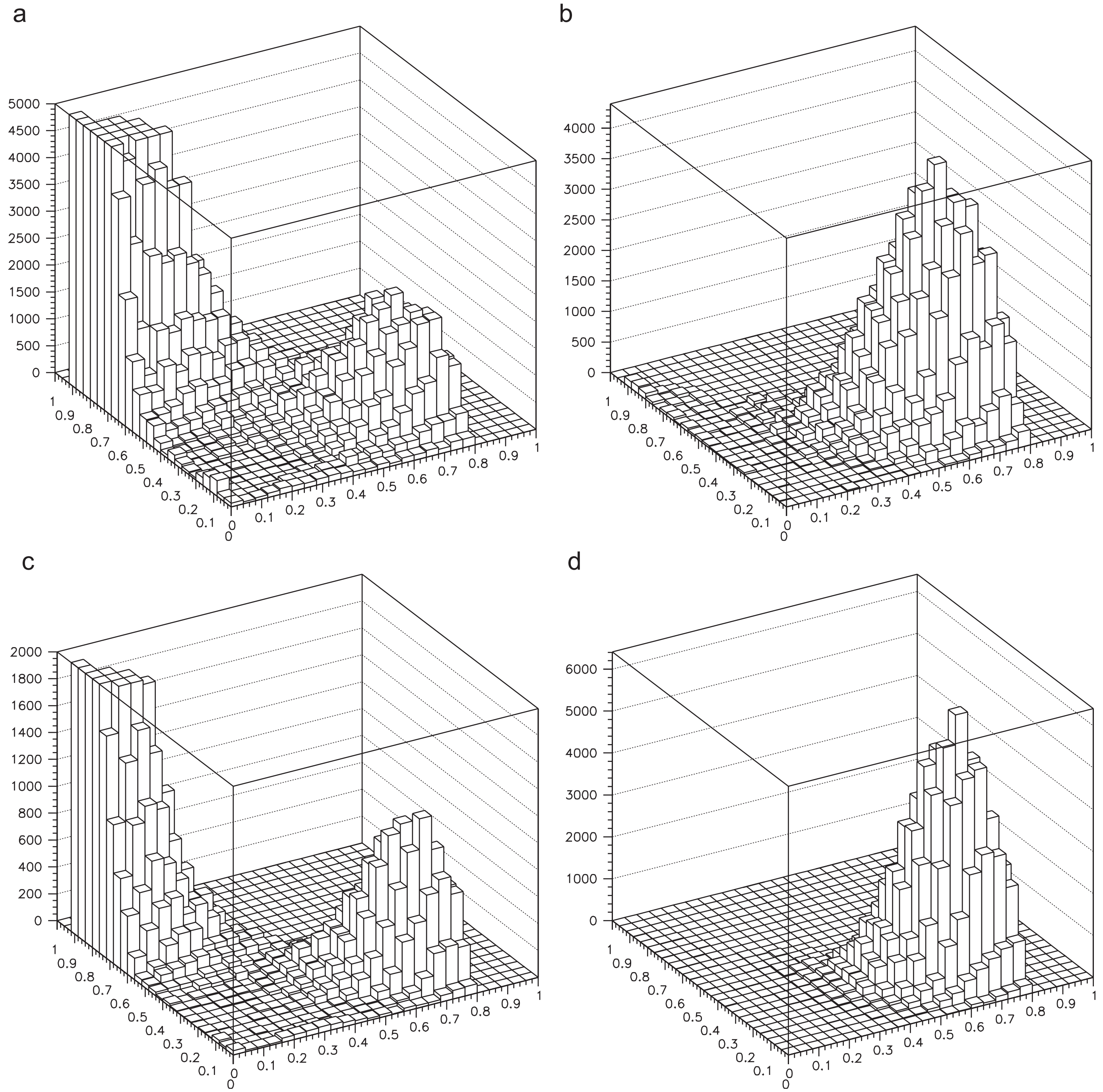

Fig. 25. Bidimensional plots in the X_1 vs. X_2 plane. The two plots on the left have been obtained for the *single-hit* production data, which contain both the PMT noise and the scintillation events. The two plots on the right have been obtained for events from a γ source of suitable strength; thus just scintillation events are present. The plots on the top refer to the 2–4 keV energy interval and those on the bottom to 4–6 keV. The noise is clearly separated from the scintillation events; see text.

offer a very effective procedure.[10] In fact, the first variable is distributed around 0 for noise events and around 0.7 for scintillation pulses; the second variable indeed is distributed around 1 for noise and around 0.25 for scintillation events.[11] The values of the two variables quoted above, obtained for each event of the production data, can be plotted one *vs* the other, as in Fig. 25(*left panels*); the signature of the residual noise above the software energy threshold with respect to the scintillation events is evident.

Thus, suitable acceptance windows can be applied to obtain just scintillation events. Fig. 25 clearly points out that stringent acceptance windows can be used to select a data sample clean from noise; the effectiveness of this procedure has already been demonstrated by DAMA/NaI [3,4].

8.5. *The overall efficiency for Dark Matter investigation*

As mentioned above, two PMTs on each detector work in coincidence at single photoelectron threshold. This—considering

---

[10] Note that the 600 ns time interval corresponds to the usual hardware gate for NaI(Tl) pulses and it is equal to $\simeq 2.5$ times the decay time of a scintillation pulse, that is the area (from 0 to 600 ns) is proportional to the energy of the event.

[11] Qualitatively, hypothesizing only one decay constant the expected value for scintillation events should be 0.64 for the first variable and $\simeq 0.2$ for the second one.

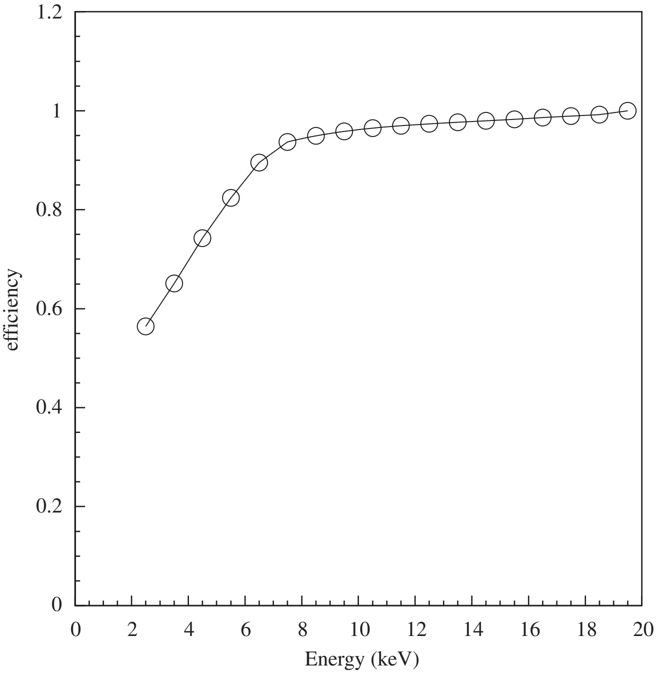

Fig. 26. Typical behavior of the overall efficiencies for the *single-hit* events. They are dominated by the efficiency related to the stringent acceptance windows used in the data analysis to assure the full rejection of noise near energy threshold (see Fig. 25); see text.

also the relatively high available number of photoelectrons/keV—assures that the required coincidence of the two PMTs does not introduce a very significant hardware cut of the events near the energy threshold. In fact, it is $\simeq 0.8$ in the 2–3 keV bin and 1 above 5 keV for a coincidence time window of 50 ns and practically always equal to unity in case of a 100 ns time window.

The efficiencies related to the used acceptance windows for the *single-hit* events in the lowest energy bins can be determined and properly used in order to account for scintillation events, that might be lost by applying the acceptance windows. These efficiencies, for each considered energy bin, are measured by applying the same acceptance windows to events induced by a ^{241}Am source of suitable activity in the same experimental conditions and energy range as the production data (see Fig. 25(*right panels*)). Thus, very stringent acceptance windows, which assure absence of any noise tail, can be considered and related efficiencies can be properly evaluated and used (see Fig. 26). In particular, to determine the efficiencies of the acceptance windows and their stability over the whole data taking periods, they are regularly measured by a suitable ^{241}Am source.[12] These routine efficiency measurements are performed roughly each 10 days; each time typically 10^4-10^5 events per keV are collected.

Let us now consider the radiation which can be induced in the crystal by the Dark Matter particles (see e.g. Refs. [4–6,8,10,11]). Also thanks to the large number of available photoelectrons and to the single photoelectron threshold of each PMT working in coincidence, the detection efficiencies for internal photons and/or X-rays in the few keV range approaches the unity as well as for electrons. The detection efficiency for nuclear recoils is practically equal to unity considering the shortness of the recoil's range in matter.

8.6. The energy threshold

As shown, the new DAMA/LIBRA detectors have been calibrated down to the keV region (see Figs. 9 and 19). This assures a clear knowledge of the "physical" energy threshold of the experiment. It obviously profits of the relatively high number of available photoelectrons/keV; the larger this number is, the lower is the reachable physical threshold. In particular, in DAMA/LIBRA the two PMTs of each detector work in coincidence with hardware threshold at single photoelectron level, while the software energy threshold used by the experiment is 2 keV. This latter value is well supported by the keV range calibrations, by the features of the near-threshold-noise full rejection procedure and by the efficiencies when lowering the number of available photoelectrons (see for example, Fig. 26).

8.7. The single-hit scintillation events at low energy

The procedure for noise rejection near energy threshold, described above, is the only procedure applied to the collected data. Fig. 27 shows, as example, the resulting cumulative low energy distribution of the *single-hit* scintillation events, as measured by DAMA/LIBRA detectors in an exposure of 0.53 ton × yr. This energy distribution is the mean value of all the used detectors; some differences among the detectors are present depending e.g. on their specific levels of residual contaminants and on their position in the matrix.

It is worth noting that—as in the former DAMA/NaI experiment—neither other on-line or off-line techniques nor backgrounds from residual radioactivity suppression are performed at all. In particular, background contribution to the counting rate of the *single-hit* scintillation events, arising from residual radioactivity in the experimental apparatus, cannot precisely be extrapolated in the keV region e.g. because of: (i) the limitation of Monte-Carlo simulation programs at very low energies; (ii) the fact that often just upper limits for residual contaminants are available; (iii) the unknown location of each residual contaminant in each component; etc. Nevertheless, the investigations, presented in previous section, are extremely useful e.g. to qualify the detectors and to identify the sources which should be reduced in further developments of radiopure crystals, detectors' components, apparatus components, etc. On the other hand, as known, the annual modulation signature, which is exploited by DAMA apparata, acts itself as an effective background rejection procedure.

8.8. Response to nuclear recoils

Finally, it is worth noting that, whenever WIMP (or WIMP-like) candidates are considered in corollary analyses of Dark Matter

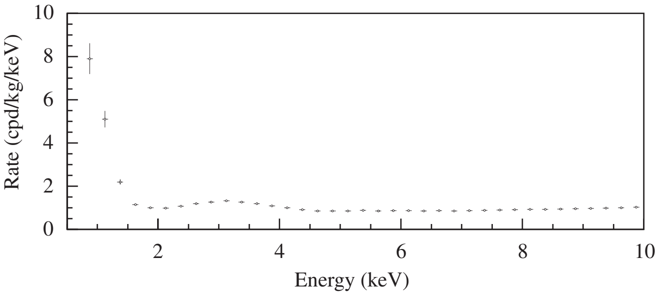

Fig. 27. Cumulative low-energy distribution of the *single-hit* scintillation events (that is each detector has all the others as veto) as measured by the used DAMA/LIBRA detectors in an exposure of 0.53 ton × yr. The energy threshold of the experiment is at 2 keV and corrections for efficiencies are already applied. See text.

---

[12] The use of ^{137}Cs Compton electron calibrations practically gives the same values as also already verified in DAMA/NaI.

investigations, the response of the NaI(Tl) detectors to nuclear recoils has to be taken into account [4]. Moreover, for a correct evaluation of the phenomenologies connected with the detection of WIMP (or WIMP-like) candidates, the so-called Migdal effect [8] and the channeling effects [9] have also to be considered. Detailed discussions can be found e.g. in Refs. [8,9].

8.9. Stability of the running conditions

As already done for DAMA/NaI (see e.g. Refs. [3,4]), the stability of several parameters and of the running conditions is monitored along all the data taking. This aspect is directly related with the experimental results on the annual modulation signature and, therefore, it will be discussed elsewhere.

9. Conclusions

In this paper, the $\simeq 250\,\text{kg}$ highly radiopure NaI(Tl) DAMA/LIBRA apparatus, running at the Gran Sasso National Laboratory of the INFN, has been described. The main components and performances have been discussed.

References

[1] P. Belli, R. Bernabei, C. Bacci, A. Incicchitti, R. Marcovaldi, D. Prosperi, DAMA proposal to INFN Scientific Committee II, 24 April, 1990;
R. Bernabei, et al., Phys. Lett. B 389 (1996) 757;
R. Bernabei, et al., Phys. Lett. B 424 (1998) 195;
R. Bernabei, et al., Phys. Lett. B 450 (1999) 448;
P. Belli, et al., Phys. Rev. D 61 (2000) 023512;
R. Bernabei, et al., Phys. Lett. B 480 (2000) 23;
R. Bernabei, et al., Phys. Lett. B 509 (2001) 197;
R. Bernabei, et al., Eur. Phys. J. C 23 (2002) 61;
P. Belli, et al., Phys. Rev. D 66 (2002) 043503.

[2] R. Bernabei, et al., Il Nuovo Cim. A 112 (1999) 545.

[3] R. Bernabei, et al., Eur. Phys. J. C 18 (2000) 283.

[4] R. Bernabei, et al., La Rivista del Nuovo Cimento 26 (1) (2003) 1.

[5] R. Bernabei, et al., Int. J. Mod. Phys. D 13 (2004) 2127.

[6] R. Bernabei, et al., Int. J. Mod. Phys. A 21 (2006) 1445.

[7] R. Bernabei, et al., Eur. Phys. J. C 47 (2006) 263.

[8] R. Bernabei, et al., Int. J. Mod. Phys. A 22 (2007) 3155.

[9] R. Bernabei, et al., Eur. Phys. J. C 53 (2008) 205.

[10] R. Bernabei, et al., Phys. Rev. D 77 (2008) 023506.

[11] R. Bernabei, et al., preprint ROM2F/2008/02, arXiv:0802.4336 [astro-ph].

[12] R. Bernabei, et al., Phys. Lett. B 408 (1997) 439;
R. Belli, et al., Phys. Lett. B 460 (1999) 236;
R. Bernabei, et al., Phys. Rev. Lett. 83 (1999) 4918;
P. Belli, et al., Phys. Rev. C 60 (1999) 065501;
R. Bernabei, et al., Il Nuovo Cimento A 112 (1999) 1541;
R. Bernabei, et al., Phys. Lett. B 515 (2001) 6;
F. Cappella, et al., Eur. Phys. J.-direct C 14 (2002) 1;
R. Bernabei, et al., Eur. Phys. J. A 23 (2005) 7;
R. Bernabei, et al., Eur. Phys. J. A 24 (2005) 51.

[13] R. Bernabei, et al., Astrop. Phys. 4 (1995) 45;
R. Bernabei, The identification of Dark Matter, World Science Publication, 1997, p. 574, in the volume.

[14] M.W. Goodman, E. Witten, Phys. Rev. D 31 (1985) 3059;
W.H. Press, D.N. Spergel, Astrophys. J. 296 (1985) 679;
R.L. Gilliland, et al., Astrophys. J. 306 (1986) 703;
K.A. Drukier, et al., Phys. Rev. D 33 (1986) 3495;
K. Freese, et al., Phys. Rev. D 37 (1988) 3388;
K. Griest, Phys. Rev. D 38 (1988) 2357;
K. Griest, Phys. Rev. Lett. 61 (1988) 666;
R. Barbieri, M. Frigeni, G.F. Giudice, Nucl. Phys. B 313 (1989) 725;
G. Gelmini, P. Gondolo, E. Roulet, Nucl. Phys. B 351 (1991) 623;
A. Bottino, V. de Alfaro, N. Fornengo, G. Mignola, S. Scopel, Astrop. Phys. 2 (1994) 77;
A. Bottino, F. Donato, N. Fornengo, S. Scopel, Phys. Rev. D 63 (2001) 125003.

[15] T. Asaka, et al., Phys. Rev. D 58 (1998) 023507;
T. Asaka, et al., Phys. Rev. D 58 (1998) 083509;
D. Smith, N. Weiner, Phys. Rev. D 64 (2001) 043502;
R. Volkas, Prog. Part. Nucl. Phys. 48 (2002) 161;
R. Foot, hep-ph/0308254.
K. Belotsky, D. Fargion, M. Khlopov, R.V. Konoplich, hep-ph/0411093;
D. Hooper, L.T. Wang, Phys. Rev. D 70 (2004) 063506;
D. Smith, N. Weiner, Phys. Rev. D 72 (2005) 063509;
S. Mitra, Phys. Rev. D 71 (2005) 121302;
C. Picciotto, M. Pospelov, Phys. Lett. B 605 (2005) 15;
M. Kawasaki, T. Yanagida, Phys. Lett. B 624 (2005) 162;
D.V. Ahluwalia-Khalilova, D. Grumiller, Phys. Rev. D 72 (2005) 067701;
D.V. Ahluwalia-Khalilova, D. Grumiller, JCAP 07 (2005) 012;
J. Knodlseder, et al., Astron. Astrophys. 441 (2005) 513;
J. M. Frére, et al., arXiv:hep-ph/0610240;
Y. Ascasibar, P. Jean, C. Boehm, J. Knoedlseder, Mon. Not. R. Astron. Soc. 368 (2006) 1695;
E.M. Drobyshevski, et al., arXiv:0704.0982 and arXiv:0706.3095;
D. Hooper, et al., arXiv:0704.2558[astro-ph];
C. Jacoby, S. Nussinov, J. High Energy Phys. 05 (2007) 017;
D.P. Finkbeiner, N. Weiner, Phys. Rev. D 76 (2007) 083519;
M. Pospelov, A. Ritz, Phys. Lett. B 651 (2007) 208;
P. Fayet, Phys. Rev. D 75 (2007) 115017;
A. Kusenko, AIP Conf. Proc. 917 (2007) 58;
A. Palazzo, et al., Phys. Rev. D 76 (2007) 103511;
M. Shaposhnikov, Nucl. Phys. B 763 (2007) 49;
M. Lemoine, et al., Phys. Lett. B 645 (2007) 222.

[16] E. Feenberg, H. Primakoff, Phys. Rev. 70 (1946) 980;
A.R. Bodmer, Phys. Rev. D 4 (1971) 1601;
A.B. Migdal, Zh. Eksp. Theor. Fiz. 61 (1971) 2209 (Sov. Phys. JETP 34 (1972) 1184);
T.D. Lee, G.C. Wick, Phys. Rev. D 9 (1974) 2291;
A.B. Migdal, et al., Zh. Eksp. Theor. Fiz. 66 (1974) 443 (Sov. Phys. JETP 39 (1974) 212);
T.D. Lee, Rev. Mod. Phys. 47 (1975) 267;
R.D. Peccei, H.R. Quinn, Phys. Rev. Lett. 38 (1977) 1440;
L.B. Okun, Ya.B. Zeldovich, Phys. Lett. 78B (1978) 597;
A.B. Migdal, Rev. Mod. Phys. 50 (1978) 107;
M.B. Voloshin, L.B. Okun, Pis'ma Zh. Eksp. Theor. Fiz. 28 (1978) 156 (JETP Lett. 28 (1978) 145);
A. Sandulescu, et al., Sov. J. Part. Nucl. 11 (1980) 528;
M. Goldhaber, P. Langacker, R. Slansky, Science 210 (1980) 851;
P. Langacker, Phys. Rep. 71 (1981) 185;
L.B. Okun, Leptons and Quarks, North-Holland, Amsterdam, 1982, p. 181;
R.N. Mohapatra, Phys. Rev. Lett. 59 (1987) 1510;
L.B. Okun, Usp. Fiz. Nauk. 158 (1989) 293 (Sov. Phys. Usp. 32 (1989) 543);
L.B. Okun, Comments Nucl. Part. Phys. 19 (1989) 99;
K. van Bibber, P.M. McIntyre, D.E. Morris, G.G. Raffelt, Phys. Rev. D 39 (1989) 2089;
R.N. Mohapatra, Phys. Lett. B 242 (1990) 407;
D. Kekez, et al., Nature 348 (1990) 224;
F.J. Yndurain, Phys. Lett. B 256 (1991) 15;
G. Dvali, G. Gabadadze, G. Senjanovic, hep-ph/9910207;
A.O. Gattone, et al., Nucl. Phys. B (Proc. Suppl.) 70 (1999) 59.

[17] M. Wojcik, Nucl. Instr. and Meth. B 61 (1991) 8.

[18] P. Belli, et al., Il Nuovo Cimento A 101 (1989) 959.

[19] M. Cribier, et al., Astrop. Phys. 4 (1995) 23.

[20] A. Rindi, et al., LNGS report LNF-88/01(P), 1988.

[21] F. Arneodo, et al., Il Nuovo Cimento A 8 (1999) 819.

[22] B. Halle, Nachfl., Suprasil data sheet.

[23] J.B. Birks, The Theory and the Practice of Scintillation Counting, Pergamon Press Ltd., London, 1967.

[24] F.A. Danevich, et al., Phys. Lett. B 344 (1995) 72;
F.A. Danevich, et al., Nucl. Phys. A 694 (2001) 375;
P. Belli, et al., Nucl. Instr. and Meth. A 498 (2003) 352.

[25] R.B. Firestone, et al., Table of Isotopes, eighth ed., Wiley, New York, 1996 and CD update, 1998.

[26] Dyers, et al., IEEE91 Th0400-2 (1991) 553.

[27] R. Silberberg, C.H. Tsao, Astrophys. J. 25 (1973) 315.

[28] U. Fehn, et al., Geophys. Res. Lett. 13 (1986) 137;
J.E. Moran, et al., Chem. Geol. 152 (1998) 193.

[29] C.M. Lederer, V.S. Shirley (Eds.), Table of Isotopes, seventh ed., Wiley, 1978.

[30] K. Hagiwara, et al., Phys. Rev. D 66 (2002) 1.